Politecnico di Torino

Master's Degree in Electronic Engineering
Department of Electronics and Telecommunications

Master Thesis

Modeling of optical modulators for optical link analysis

Optical link analysis in silicon photonics technologies

Supervisor:
Prof. Mariangela GIOANNINI
Co-Supervisor:
Prof. Giovanni GHIONE

Internship Advisor:
PhD. Eng. Nicolas PANTANO

Candidate:
Daniele POGGI

2018/2019

Abstract

According to the Ethernet Roadmap projections, the requirements for high speed links keep increasing every year, always considering the energy consumption per bit of the communication system as a significant factor. The Ethernet requirements are estimated to reach $1Tbps$ by 2022-2025.

Optical links are a concrete solutions to satisfy bandwidth requirements at low energy consumption. An optical link is a communication system that consists of a single end-to-end optical circuit. In contrast with vertical-cavity surface-emitting laser (VCSEL) technology, which is based on a direct laser modulation, silicon photonics technology (SPT) is based on indirect modulation and can lead to many advantages such as C-MOS compatibility, integration and low costs. In order to perform a modulation in SPT, electro-optical modulators are needed in the optical link system for electrically modulating the optical power.

This master thesis, developed at IMEC, will present the modeling of two different technologies of optical modulators: the Silicon Ring Modulator and the Franz-Keldysh Electro-Absorption Modulator. After having studied the physical working principles, the models for these two modulators were realized, in order to complete the IMEC models framework of silicon photonics technologies for performing optical link analysis. Firstly, it was performed a preliminary study of the physical principles of the two devices in order to build the MATLAB models. Then, these models were fitted with measurements, in order to adjust the characteristics to a real-life behaviour. After having obtained two working models of the two modulators, it was used an already-existing framework, to compare the energy per bit consumption in the optical link. In the end, the results obtained with the simulations were presented and discussed.

Keywords:

Silicon photonics, physical modeling , ring modulator, electro-absorption modulator, optical modulator, optical link system, power consumption

Table of contents

List of figures

List of tables

List of acronyms and abbreviations

CMOS Complementary Metal Oxide Semiconductor

EAM Electro-Absorption Modulator

ER Extinction Ratio

FK Frantz-Keldysh Effect

FOM Figure Of Merith

FSR Free Spectral Range

FWHM Full Width at Half Maximum

I/O Input/Output

IL Insertion Loss

ME Modulation Efficiency

NRZ Non Return to Zero

PAM Pulse Amplitude Modulation

OMA Optical Modulating Amplitude

QCSE Quantum Confined Star Effect

RM Ring Modulator

SPT Silicon Photonics Technology

TIA Trans-Impedence Amplifier

TP Transmission Penalty

WDM   Wavelength Division Multiplexing

1 **Introduction**

This introductory chapter describes the motivation of this master thesis work, starting from the background in the photonics topic and motivating the need to reach high Input/Output (I/O) bandwidth in communication systems. Thus, the technologies to achieve high I/O bandwidth are briefly presented, considering the silicon photonics technology (SPT) as a valid option. In the last sections of this chapter it is described the thesis outline and contribution to the SPT topic.

1.1 | Problem description

Nowadays, according to F.O'Mahony *et al.* study [1], electrical interconnections are the main limiting factor in the whole system performances. One of the main reason for this limitation in high-speed in I/O data rate is the fact that the electrical frequency characteristics depend on the channel length. Moreover, at high-speed (above 10 Gb/s) the cross-talk effects require shielding and differential solutions, which result in an increase of the area occupied by the interconnections in the chip. For future chip-to-chip requirements, it is necessary to increase the performances (in terms of bit-rate), but also considering the energy efficiency of the link system. According to the Ethernet Roadmap projections presented by the Ethernet Alliance, communication speeds need also to increase in terms of bandwidth [2]. In particular, it is stated: "the standard is continually evolving to meet the needs of worldwide industry [...] IEEE provides the forum for the global Ethernet ecosystem to come together to make such progress. Through the new IEEE 802.3 400 Gb/s Ethernet Study Group, individuals from end users, equipment vendors, [...] and consultants from across all geographic regions worldwide are invited to participate in shaping the future of Ethernet's potential new higher-speed standards-development efforts". In figure 1.1, are shown the projections for the bandwidth

requirements up to 2030 according to the Ethernet Alliance roadmap.
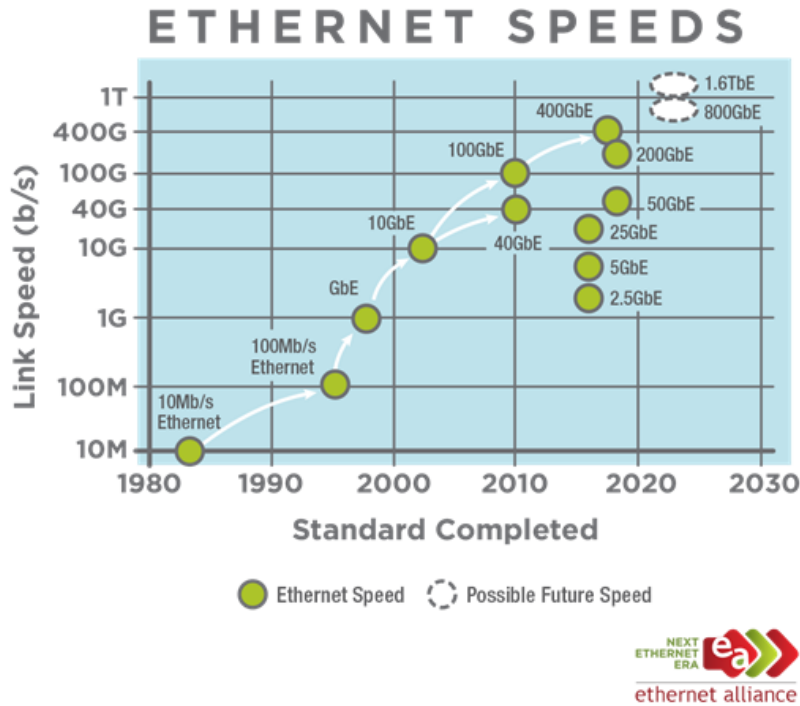
Fig. 1.1 Projections of Ethernet Alliance of link speed requirements up to 2030 [3].

1.2 | Optical link system

In order to overcome the limitations of I/O bandwidth, several technology solutions are being studied, in order to guarantee the increasing of high speed performances at a sustainable energy efficiency in the near future. The optical link is the solution that is able to satisfy the requirements above 100 *Gbps*, as documented in [4], [5].

There are two main optical technologies that compete to overcome the issues mentioned [6], the vertical-cavity surface-emitting laser (VCSEL) and the silicon photonics technology (SPT)[7]. The main advantages of the VCSEL are the small sizes, which provide low power consumption and high performances with a direct light modulation. This technology is stated to be better for distances around hundreds of meters [8] and works at wavelengths around 850 *nm*. On the other hand, SPT uses an indirectly modulated external laser source, thus requires the usage of an *optical modulator*, and with this technology different advantages can be achieved, as already demonstrated [6]. SPT can work at wavelengths of 1300 *nm* (o-band),

or at 1550 *nm* (c-band). Furthermore, SPT allows scalability and CMOS compatibility, according to the projections of the International Technology Roadmap for Semiconductors (ITRS). A block diagram of the SPT system is shown in figure 1.2. The optical link system is formed of a laser, which generates an optical power at the desired working wavelength. The laser it the first block of the transmitter, however it has been put outside of the chip, since it is very difficult to integrate it in the chip. The light of the the laser is then coupled to a waveguide, through a grating coupler. The optical power is then modulated with the usage of an *optical modulator* which is driven with an electrical signal, and then sent out of the chip. An optical fiber brings the optical signal to the receiver chip. The light is converted in current with a photo-detector and then a transimpedance amplifier (TIA) converts the current into voltage. At the end of the link, a limiting amplifier sets the dynamics of the voltage swing to the desired one.

The usage of STP allows transmission of the optical signals with low losses at the optical wavelengths. There are two main bands used in the optical domain which are 1310 nm, also called O-band (original band) and 1550 nm, called c-band (conventional band). The region of interest of this thesis work will be the c-band region.
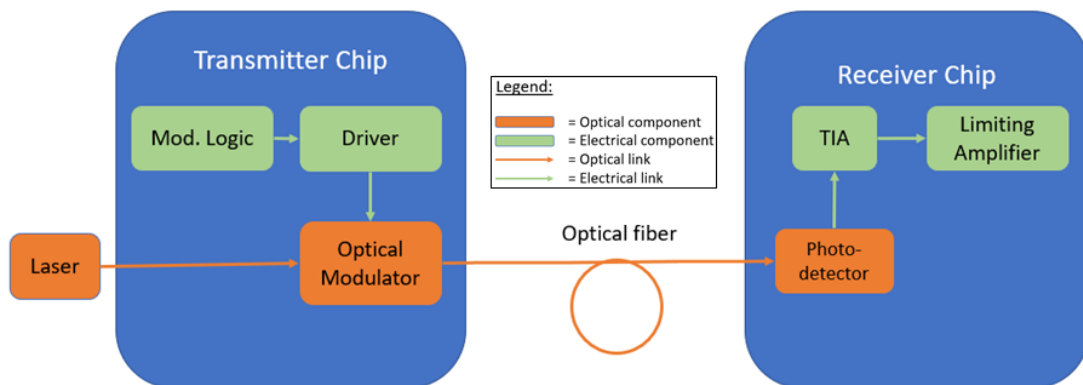
Fig. 1.2 Block diagram of the optical link system, distinguishing electrical from optical blocks.

As already said, SPT is based on indirect modulation, which means that an electro-optical modulator is necessary in the system, as visible in figure 1.2. There are different structures and technologies, for implementing an optical modulator. In [6] is presented the study of an optical link system with a *Silicon ring modulator* (Si RM), with some results obtained with a transceiver demonstrator implemented at IMEC. However, other modulator structures can be the*Mach-Zehnder Interferometer* (MZI) and the *Electro Absorption Modulator* (EAM) [9]. This last type of modulator, can be based on two physical principles: the Franz-Keldysh effect (FK-EAM) [10] or on the Quantum Confined Star Effect (QCSE-EAM). With respect

to the Si RM and the MZI, in which the indirect modulation is performed by constructive or destructive interference by the variation of the n_{eff} with the applied voltage (also called *plasma effect*), the EAM modulation is based on the changing of the absorption in the semiconductor, by applying an electric field.

The MZI and QCSE-EAM will not be presented in this work. In fact, the MZI is already very present in literature and leads to many advantages, such as the performances of the device. However, the main problems of this device are its very large footprint area and high driving voltage and input capacitance, which lead to a very high power consumption. The QCSE-EAM is, instead, an emerging technology very sensitive to process variations, and for this reason it is very difficult to obtain a well-performing device demonstrator.

On the other hand, a Si RM leads to many advantages: small dimensions and high integrability, high performances and low parasitics effect. Moreover, it can operate at low-voltage, which means that it is compatible with CMOS circuit drivers and has thus a low power consumption. Another advantage of this structure is the very small optical 1dB bandwidth, which can allow wavelength division multiplexing (WDM), thus increasing the performances in terms of bit-rate per channel.

However, the Si RM is very sensitive to temperature (high thermal drift $TD\ [nm/K]$) and very low thermal efficiency, which means that heaters consume a lot of power to keep the structure in the desired working condition, and thus the energy efficiency of the system decreases. The heater of the Si RM has also a large area, thus its dimensions impact on the total area of the chip. For this reason, the FK-EAM is an alternative structure for the optical modulator, that is interesting to compared with the Si RM, in order to understand if one structure can allow the best trade-off between performances and power consumption to the optical system.

1.2.1 | Silicon Photonics technology

The European Commission has identified *photonics* as one of the *key enabling technologies* (KETs) of the 21st century, under the EU's new Research and Innovation (R&I) framework programme for 2014-2020 (Horizon 2020) [12]. One of the most concrete technologies to investigate in the field is *silicon photonics technology* (SPT), as already specified in the previous sections. The large usage of Silicon allows the integration with CMOS very large scale integration (VLSI), and for this reason silicon photonics is said to be "the most active discipline within the field of integrated optics" [13].

The possibility of integrating electronics and photonics on the same chip with SPT can also increase the energy efficiency of the system, by reducing the parasitics effects. "The advantages of CMOS photonics for next generation transceiver applications have been

outlined in terms of raw bandwidth, channel capacity, reach, power, cost, link performance and reliability" [7].

The main goal for on-chip optical interconnects, is the realization of an high-speed link with a good energy efficiency ($10fJ/bit - 100fJ/bit$) [14]. The next step is then to obtain models for the different components for simulating the optical link system, to understand if SPT can in the near future be a concrete alternative to overcome badwidth limitations.

1.3 | Research objective and contribution

The main objective in this research was to obtain models for the Si RM and FK-EAM optical modulators, in order to simulate the optical link, since no available model for this component was present in IMEC framework. In particular, one of the most important parameters to consider in the models was the temperature dependency, since these devices are very dependent on it. Several SPT performances have already been demonstrated, and the possibility to reduce the energy consumption per bit (J/bit) with this technology, keeping the bandwidth increasing, is a key feature that has to be studied in depth. The possibility of reducing power consumption for link interconnects, by also increasing the speed, makes the SPT an interesting area of research for overcoming the current limitations. For studying its advantages in an accurate way, the modeling of the different blocks of the optical link have to be realized. One of these fundamental blocks is the *optical modulator*.

The main work developed in this thesis consisted in obtaining Silicon Ring modulator (Si RM) and the Franz-Keldysh Electro-absorption modulator (FK-EAM) models, to simulate the optical link system and to evaluate its performances and energy consumption per bit. For this purpose, the physical working principles of the two structures have been studied and the models realized, taking into account the temperature dependency of the models; after this step, it was performed a fitting of the models with some provided IMEC measurements of the devices. In the end, the total energy efficiency of the optical link system with the two modulators was compared, in order to decide which is the best solution to adopt.

1.4 | Outline of the thesis

This master thesis is divided in 6 chapters. In **Chapter 1**, it was presented the theoretical background of I/O bandwidth limitations. SPT was then described to be one of the possible solutions to overcome the problem and it will be matter of analysis in the next chapters.

In **Chapter 2** it is described the Si RM, as one of the possible technological implementations for the optical modulator. Firstly, a simulation of the already-existing IMEC Si RM model on Lumerical Interconnect is performed, and the exploitation of the main figures of merit (FOMs) is done, to clarify the terminology and the main parameters that characterize this device. After, some relevant limitations of the existing Lumerical Interconnect compact model are highlighted and the need of a more flexible but still accurate model is pointed out. Thus, a description of the device physical working principle is presented, followed by the realization of a Si RM MATLAB model. In the end, the model is fitted with IMEC measurements, in order to have a model based on real Si RM performances.

In **Chapter 3**, the same methodology applied in chapter 2 is repeated for the GeSi FK-EAM. This device is an alternative technological implementation of the modulator. As done in the previous chapter, a MATLAB modeling was realized, after having performed a study of the physics of the device. In the end, the model was fitted with IMEC state-of-the-art measurements.

Chapter 4 contains the evaluation of the energy per bit of the optical link system, adding the two models implemented in the previous sections to an already-existing framework, under different conditions, to understand which is the optimum modulator to use in the link.

In **Chapter 5**, the most interesting results of the previous chapters are summarized and discussed.

In the end, **Chapter 6** contains a dissertation about this research work, pointing out some outcomes about the previous chapters and some conclusions that were carried out. The chapter ends with presenting possible future work related to this thesis.

2 Ring Modulator

The first optical modulator that was implemented was the Silicon ring modulator (Si RM). A ring modulator is a device based on a ring resonator structure, which is made of a group of waveguides which couple light into a closed loop. At the intersection between the ring and the waveguide (as shown in figure 2.1), part of the light is self-coupled through the waveguide and another part is cross-coupled in the ring. The self coupling coefficient (called t), while the cross-coupling coefficient (named k). In case of no-losses it is valid that $|t|^2 + |k|^2 = 1$.
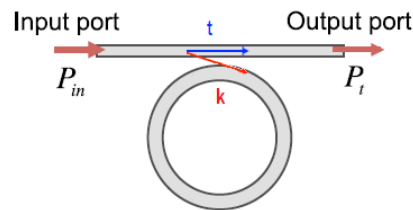
Fig. 2.1 Schematic of the ring modulator.

The silicon ring modulator physical working principle (which will be described more in depth in section 2.2) is the *plasma effect*, which allows the variation of the effective refractive index (n_{eff}) of the waveguide, depending on the voltage applied on the p-n junction, as it also happens in the Mach-Zehnder Interferometer (MZI). Due to this principle, the transmitted optical power (P_t) depends on the applied voltage, and in this way the light can be modulated. The transfer function can be written as $T_n(\lambda, V) = P_t/P_{in}$, where P_{in} is the optical power at the input of the RM (fig. 2.1).

The ring modulator reaches the resonance condition at λ_r, when the round trip phase shift between two waves ($\theta = \beta L$) is an integer multiple of 2π, which means:

$$\theta = \beta L = 2\pi m, \; with \; \beta = \frac{2\pi n_{eff}}{\lambda} \rightarrow \lambda_r = \frac{L n_{eff}}{m}$$

The main advantage of this kind of modulator is its small dimensions, which are also necessary to achieve a large free spectral range (*FSR*). In fact, as stated in [15], the free spectral range of this kind of device is inversely proportional to the length (*L*) of the ring:

$$FSR = \frac{\lambda_r^2}{L n_g}$$

where λ_r is the resonating wavelength of the ring modulator, n_g is the group index and $L = 2\pi R$ is the round trip length of the ring (with R as the ring radius). For example, considering to work in the C-Band, with $\lambda_r \approx 1.55 \; \mu m$ and considering a group index $n_g = 3.9$ (values expressed in paper [15]), to achieve at least $FSR = 20 \; nm$, it is necessary to have a ring radius of no more than $R \approx 5 \; \mu m$.

The second advantage of the ring modulator is its very narrow optical bandwidth, which can allow the wavelength division multiplexing (WDM). The optical bandwidth can be defined as the full width at half maximum (*FWHM*), as stated in [15]:

$$FWHM = \frac{(1 - ta)\lambda_r^2}{\pi n_g L \sqrt{ta}}$$

where t is the self-coupling factor and $a = e^{-\frac{\alpha}{2}L}$ is the round trip loss (with α as the absorption coefficient). Typical values of the FWHM for this kind of device is of the order of hundreds of *pm*.

Another important aspect of the Si RM is its low power consumption. According to [6], the MZI structure has a capacitive load of at least $1 \; pF$ and requires driving voltages of at least $2 \; V_{pp}$, which means an energy per bit of $\sim 1 \; pJ/bit$ (by using the formula $E_{bit} = C_d V_{pp}^2 / 4$ in [16]). On the other hand, the small size of the Si RM and the lower swing voltage needed allow a power consumption of just few fJ/bit, as documented in [6].

After having presented some advantages of the Si RM, firstly a preliminary simulation was performed on the already-existing Lumerical Interconnect compact model. However, at the end of this analysis, some limitations of the Lumerical Interconnect available model will

be carried out in 2.1. Since a more flexible model for the Si RM, in section 2.2 it will be presented a MATLAB model for the Si RM.

2.1 | Ring modulator in Lumerical Interconnect

A first approach on the study of the Si RM was performed in Lumerical Interconnect. This software allows accurate optical simulations. Moreover, a Lumerical Interconnect model library was already existing and some models for optical components were already implemented, such as the IMEC Si RM. After getting use to this new software, a simulation set-up (shown in figure 2.2) was set and used to obtain the transmission spectra (T_n) of the ring modulator. The transmission spectra is the most important characteristic of the Si RM and depends on its wavelength and applied voltage. Reminding that the transfer function is defined as:

$$T_n = T_n(\lambda, V) = \frac{P_t}{P_{in}}$$
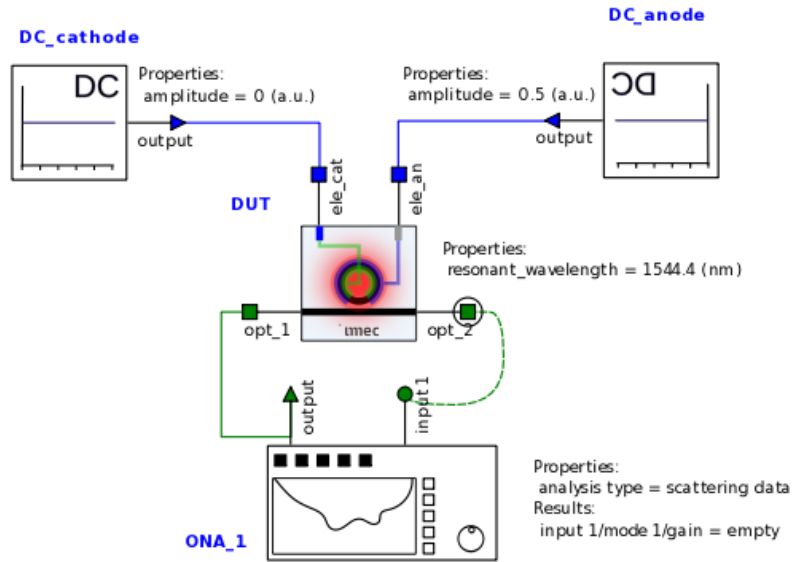
Fig. 2.2 Set-up in Lumerical Interconnect of the Si RM.

The modulated output powers P_0 and P_1 can be obtained as:

$$P_0 = P_{in} \cdot T_n(\lambda, V_0) \qquad P_1 = P_{in} \cdot T_n(\lambda, V_1)$$

From the transfer function (T_n), all the interesting *figures of merit* (FOMs) such as the insertion loss (*IL*), the extinction ratio (*ER*) and the optical modulating amplitude (*OMA*) can be computed, as it will be defined and extracted in section 2.1.1.

With the described simulation set-up, the following default parameters were set. The input power, for simplicity, was set to $P_{in} = 1\,mW$, so that $P_{in,dB} = 0\,dBm$. The cathode voltage was kept constant to $V_{cat} = 0\,V$, while for the anode voltage it was performed a sweep in the range $V_{an} = [0, 0.25, 0.5, 0.75, 1]V$ and the reverse bias voltage is defined as $V_r = V_{cat} - V_{an}$. The wavelength was run in the C-band between 1543.8 *nm* and 1545 *nm* at the temperature $T = 300\,K$. The obtained T_n is visible in figure 2.3.
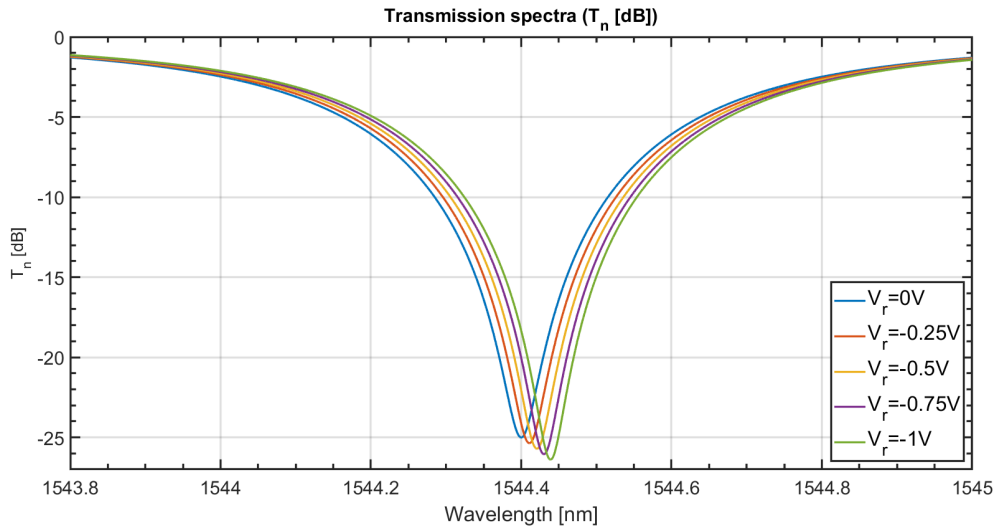
Fig. 2.3 Transmission spectra obtained from Lumerical Interconnect of the IMEC Si RM.

2.1.1 | Description of the most interesting FOMs

Once having obtained and stored in a *.mat* file the transmission spectra T_n in figure 2.3, some interesting FOMs of the RM could be extracted.

Before presenting the obtained values, it is necessary to explain what each one of them represents, in order to clarify the nomenclature (already present in literature).

First of all, the *optical modulating amplitude* (OMA), is defined as the difference between the transmitted power for an optical "logic 1" ($P_1 = P_1 = P_{in} \cdot T_n(\lambda, V_1)$) and "logic 0"

$(P_0 = P_0 = P_{in} \cdot T_n(\lambda, V_0))$:

$$OMA = P_1 - P_0 \rightarrow OMA_{dBm} = 10\log_{10}\left(\frac{P_1 - P_0}{1mW}\right)$$

From the OMA, it can be easily computed the transmission penalty (TP), which is defined as:

$$TP = \frac{P_{in}}{P_{avg}} = \frac{2P_{in}}{OMA}, \text{ where } P_{avg} = \frac{P_1 - P_0}{2}$$

$$\downarrow$$

$$TP_{dB} = -10\log_{10}\left(\frac{OMA}{2P_{in}}\right) = -OMA_{dBm} + 3.01dB + P_{in,dBm}$$

where $P_{in,dB,} = 0dBm$, since in the simulation it was set $P_{in} = 1mW$. This unitary value will be kept from now on, for all the simulations relative to this chapter.

Another important FOM is the extinction ratio (ER), defined as the ratio:

$$ER = \frac{P_1}{P_0} \rightarrow ER_{dB} = 10\log_{10}\left(\frac{P_1}{P_0}\right)$$

The last FOMs is the insertion loss (IL), which is simply computed as:

$$IL = \frac{P_{in}}{P_1} \rightarrow IL_{dB} = -T_{n,dB}, \text{ because } P_{in,dBm} = 0dBm$$

All the FOMs described, that characterize the modulation of the optical signal, can be visualized on the theoretical eye diagram shown in figure 2.4.
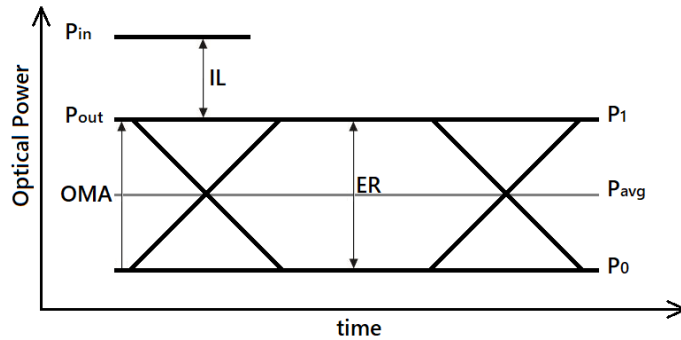
Fig. 2.4 Visualization on an ideal eye diagram of the FOMs presented in this chapter.

It is important to specify that it was considered for the "logic 0" $V_0 = 0\,V$ and for the "logic 1" the negative voltage sweep $V_1 = V_r$. **This assumption will be kept during all**

the dissertation. Moreover, after having computed the *OMA*, the OMA_{max} for each V_r was computed. The reason is because maximising the *OMA* it is maximised the difference $P_1 - P_0$.

2.1.2 | Limitations of Lumerical Interconnect model

The IMEC Si RM simulation performed in Lumerical Interconnect presented in the section above, showed up some big limitations. The biggest problem was that most of the models present in the IMEC lcml (*Lumerical compact model library*) are based on measurements, thus the models are valid only in the range of the measurements or cannot be simulated out of that ranges. For example, one of the main problems of the Si RM was said to be its strong dependency on temperature and with the available model, the temperature couldn't be varied from 300 K.

Moreover, the IMEC components in Lumerical Interconnect are encrypted and cannot be modified without special authorizations. This means that the models cannot be accessed or varied and this is a big limitation for the purpose of SPT studies. In order to overcome the problem, a physical model of the ring modulator had to be implemented and the methodology used will be discussed in section 2.2.

2.2 | Modeling the Si RM

As already mentioned in the section above, the usage of Lumerical Interconnect for simulating the Si RM led to many limitations. For this reason, a more flexible model of it needed to be implemented. The choice of the software to use for this modeling was MATLAB, for two main reasons. The first one is because of the previous knowledge of the software and the availability of its licence. The second one, was the fact that MATLAB can be used for co-simulating with Lumerical Interconnect and can be exploited in already-existing frameworks for optical link simulations that will be presented in chapter 4.

The top view of a ring modulator structure is shown in figure 2.5. The ring modulator is an optical device formed by of a waveguide which receives an input optical power (P_{in}). Part of the light keeps flowing through the waveguide. Another part is cross-coupled in the Si Ring resonator structure of a quantity proportional to the cross-coupling coefficient k. The light coupled into the ring structure, flows around the round trip length $L = 2\pi R$ (with R the ring radius) and arrives again to the initial position with a round trip phase shift θ and a round trip loss a. These two quantities depend on the wavelength and the voltage applied to the p-n

junction. As already done, from now on the cathode voltage will be considered equal to 0 V, while the anode voltage will be $V_{anode} = -V_r$.

As described in [17], the main characteristic of a ring modulator is its transmission spectra (T_n), which can be expressed as:

$$T_n = T_n(\lambda, V) = \frac{P_t}{P_{in}}, \text{ where } P_t = \left| \frac{t - e^{-\alpha_f L + i\theta}}{1 - te^{-\alpha_f L + i\theta}} \right|^2$$

where t is the self-coupling coefficient, $\alpha_f = \alpha/2$ is the field absorption coefficient, L is the length of the ring modulator and θ is the round trip phase shift. For the implementation of the ring resonator, some initial hypothesis on the parameters had to be made.

First of all, some of the technology parameters for the simulations had to be set, according to the paper [17]. It was then set a round trip length $L = 30\mu m$, so that other parameters experimentally fitted and present in the same paper could be used. In particular, the group index was set to $n_g = 3.98$, the confinement factor $\gamma = \frac{P_{core}}{P_{tot}} = 0.83$, the self-coupling coefficient $t = 0.985$, the length of the pn-junction (lateral junction assumption as shown in figure 2.5) $W = L_j = 500 \ nm$. The doping concentrations were set to $N_A = N_D = 1 \cdot 10^{18} cm^{-3}$. Some other parameters were considered to be valid at $T_0 = 300 \ K$ and $\lambda_0 = 1544.4 \ nm$, in particular: the intrinsic effective refractive index $n_{eff,i} = 2.68$ and the absorption coefficient $\alpha_i = 100m^{-1}$.
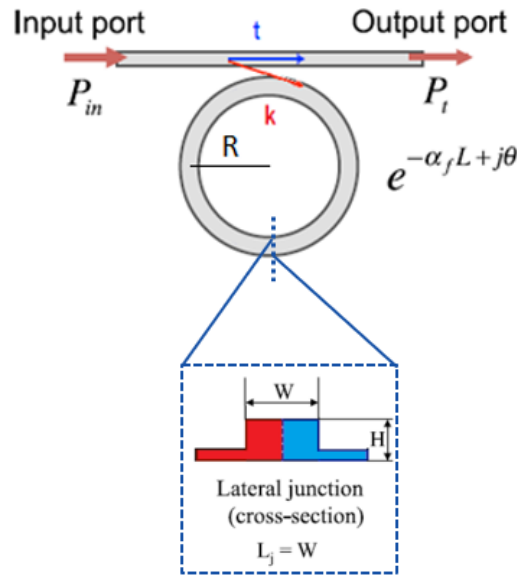
Fig. 2.5 Top view and lateral junction section of a Si ring modulator.

The the intrinsic carrier concentration was set to $n_i(300\,K) = 1.45 \cdot 10^{10}\,cm^{-3}$, from [19]. Then, the built-in potential could be computed as:

$$V_{bi}(T_0) = \frac{k_B T_0}{q} \ln \left(\frac{N_A N_D}{n_i(T_0)^2} \right) = 1.004\,V$$

In order to obtain the transfer function T_n, it was decided to perform a voltage sweep from $V_r = -1\,V$ to $V_r = 0\,V$ with a 0.25 V step and a wavelength sweep from 1544 nm to 1546 nm.

As stated in [17], the depletion widths can be computed as:

$$x_n(V) = \sqrt{\frac{2\varepsilon N_A(V_{bi} - V)}{q N_D(N_A + N_D)}} \qquad x_p(V) = \sqrt{\frac{2\varepsilon N_D(V_{bi} - V)}{q N_A(N_A + N_D)}}$$

For what concerns the variation of the effective refractive index and the absorption, it was computed the intermediate effective index $n_{eff,d}$ and absorption α_d, as done in [17]:

$$n_{eff,d} = n_{eff,i} - \gamma(A\lambda^2 N_D + B\lambda^2 N_A^{0.8})/2 \qquad \alpha_d = \alpha_i + \gamma(C\lambda^2 N_D + D\lambda^2 N_A)/2$$

where γ is the confinement factor ($0 < \gamma < 1$), the factors A, B, C, D are fitting parameters from Soref & Bennett, 1987 (in $[cm]$):

$$A = 3.64 \cdot 10^{-10} \quad B = 2.51 \cdot 10^{-6} \quad C = 3.52 \cdot 10^{-6} \quad D = 2.4 \cdot 10^{-6}$$

Moreover, it was also taken into account the fact that the intrinsic effective refractive index depends on the wavelength [17]:

$$n_{eff,i}(\lambda) = n_{eff,i}|_{\lambda_0} + \frac{\lambda - \lambda_0}{\lambda_0} \cdot (n_{eff,i}|_{\lambda_0} - n_g)$$

Then, the effective refractive index and the absorption coefficient depending on the reverse bias were computed as:

$$n_{eff}(V) = n_{eff,d} + \frac{\gamma}{L_j}(A\lambda^2 N_D x_n(V) + B\lambda^2 N_A^{0.8} x_p(V))$$

$$\alpha(V) = \alpha_d - \frac{\gamma}{L_j}(C\lambda^2 N_D x_n(V) + D\lambda^2 N_A x_p(V))$$

The results of the MATLAB implementation of n_{eff} and α for the different applied voltages was displayed in 2.6. It is important to highlight that every time that new parameters were included in the model, some intermediate plots were performed to debug the model in a correct and efficient way.

14
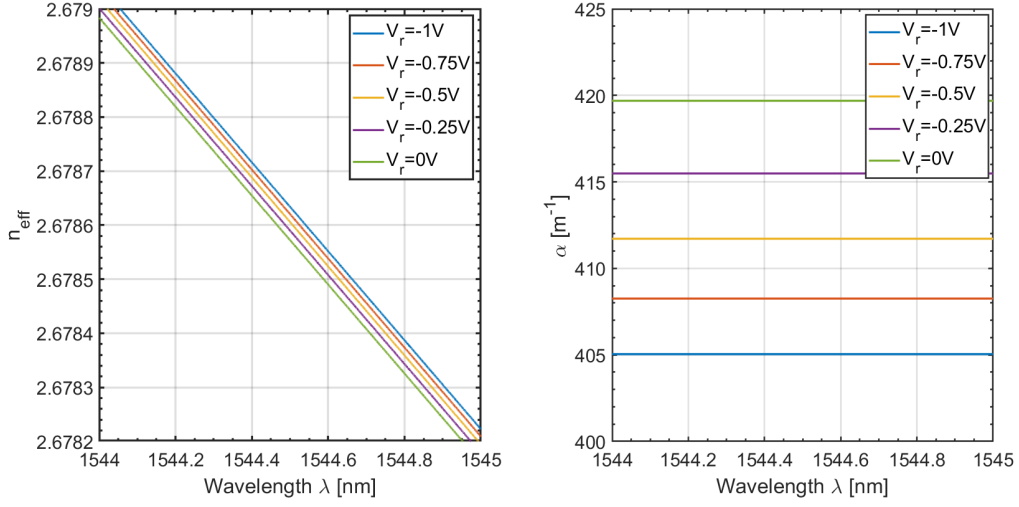
Fig. 2.6 n_{eff} and α vs λ at different reverse bias voltage V_r.

At this point, once having obtained all the main parameters, the gain (or transfer function) $T_n = \frac{P_t}{P_{in}}$ could be plot, by computing:

$$a(\lambda, V) = e^{-\alpha_f L} = e^{\frac{-\alpha(\lambda, V)}{2}L}$$

$$\theta(\lambda, V) = \frac{2\pi L n_{eff}(\lambda, V)}{\lambda}$$

In the end, remembering that the input power was set to $P_{in} = 1mW$, the transfer function of the ring modulator was computed as:

$$T_n(\lambda, V) = \left| \frac{t - e^{-\alpha_f(\lambda, V)L + i\theta(\lambda, V)}}{1 - te^{-\alpha_f(\lambda, V)L + i\theta(\lambda, V)}} \right|^2 = \left| \frac{t - a(\lambda, V) \cdot e^{+i\theta(\lambda, V)}}{1 - t \cdot a(\lambda, V) \cdot e^{i\theta(\lambda, V)}} \right|^2$$

2.2.1 | Definition and evaluation of the spectral characteristics

Once having obtained a working model, the definition of some spectral characteristics are presented. First of all, the resonant mode m ($m \in \mathbb{N}$) can be computed as

$$m = round\left(\frac{L n_{eff}}{\lambda_r} \right) = 52$$

15

After, according to [17], the resonant wavelength can be computed as:

$$\lambda_r = \frac{Ln_{eff}}{m} = 1545.1 \; nm$$

With the obtained values, one of the most important spectral characteristics of the RM could be evaluated, the theoretical *free spectral range* (*FSR*):

$$FSR = \frac{\lambda_r^2}{Ln_g} = 20.1 \; nm$$

Moreover, it was also possible to compute the *full width at half maximum* (*FWHM*) as:

$$FWHM = \frac{(1 - t \cdot a(\lambda_r, V = -1V))\lambda_r}{\pi n_g L \sqrt{t \cdot a(\lambda_r, V = -1V)}} = 210.6 \; pm$$

The resonant wavelength obtained from the plot was instead $\lambda_r = 1545.00 \; nm$, which is different from the computed wavelength of 1545.1 nm, since in the formula it was neglected the dependency of n_{eff} from the wavelength itself. For this reason, the spectral characteristics measured from the plots (figure 2.7) were slightly different and were computed to be $FSR = 19.9 \; nm$ and the $FWHM = 208.5 \; pm$ at $V_r = -1 \; V$ and $T = 300 \; K$.
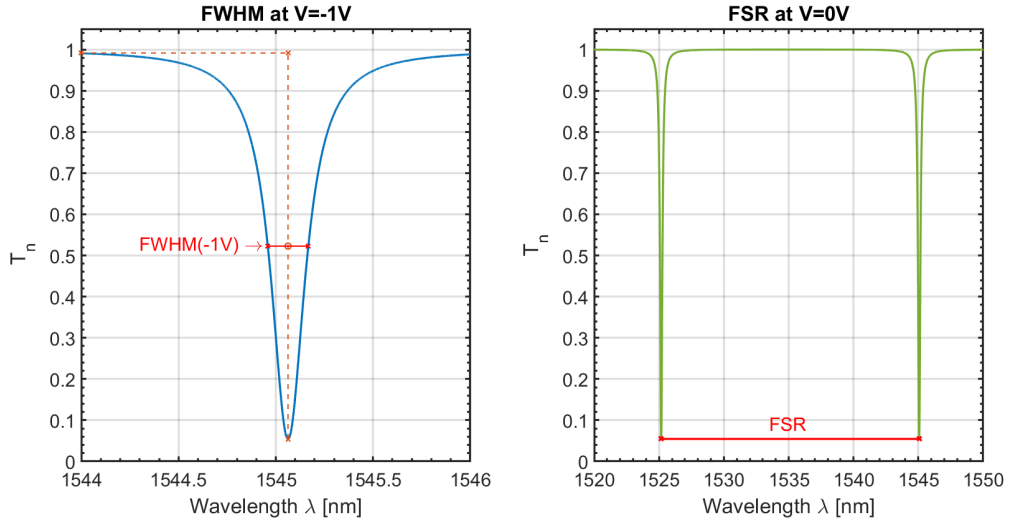
Fig. 2.7 $FWHM(-1V)$ and FSR obtained from the plot at 300K.

2.2.2 | Modeling of temperature dependency

Once having obtained a working model of the ring modulator, it was also taken into account its dependency on the temperature. This was a key aspect in this thesis work, since this

temperature effect was not implemented in other models available in literature and it is a very important factor. In fact, the optical modulators presented in this thesis are very sensitive to temperature variations and so this factor has to be modeled. On the other hand, thanks to this high sensitivity, *heaters* are used for adjusting their behaviour from eventual process variations.

To start, it had to be considered which parameters were depending on the temperature. It was started to be considered the intrinsic carrier concentration as $n_i = n_i(T)$, with the formula proposed in [19]:

$$n_i(T) = 2 \left(\frac{2\pi k_B T}{h^2} \right)^{3/2} \cdot (m_e^* \cdot m_h^*)^{3/4} \cdot e^{-E_g/(2k_B T)}$$

where m_e^* and m_h^* are the effective masses of electrons and holes. Then it was also considered that in the formula above, the energy gap is $E_g = E_g(T)$ is, as suggested in [20]:

$$E_g(T) = E_{g0} - \frac{a \cdot T^2}{T + b}$$

where $E_{g0} = E_g(0\,K)$, and a, b are fitting parameters respectively equal to:

$$E_{g0} = 1.166\,eV \qquad a = 4.73 \cdot 10^{-4}\,eV/K \qquad b = 636\,K$$

Therefore, also the reverse bias voltage V_{bi} depends on the temperature, as:

$$V_{bi}(T) = \frac{k_B T}{q} \ln \left(\frac{N_A N_D}{n_i(T)^2} \right)$$

However, implementing these temperature effects on the parameters in the range between $300\,K$ to $375\,K$, it was not experienced a significant variation in the characteristic. In particular, it was not obtained the expected wavelength shift with temperature stated in [21]. For this reason, it could be assumed that the effect of the temperature on $n_i(T), E_g(T)$ and on $V_{bi}(T)$ is negligible for the transmission spectra.

The remaining parameter that depends on the temperature is the effective refractive index. For the variation of the refractive index, it was used an experimental temperature dependency in the intrinsic effective refractive index as it follows:

$$n_{eff,i}(T) = n_{eff,i}|_{T_0} - \Delta T \cdot \frac{\partial n_{eff}}{\partial T}$$

where $\frac{\partial n_{eff}}{\partial T} = 2.05 \cdot 10^{-4}\,K^{-1}$ (according to [21]), and $\Delta T = T - T_0$ is the temperature variation with respect to the temperature T_0 at which the known intrinsic refractive index

parameter is given.

Considering that $n_{eff,i}|_{T_0} = 2.68$ at $T_0 = 300\,K$, the linear behaviour of the effective refractive index with the temperature is shown in figure 2.8.
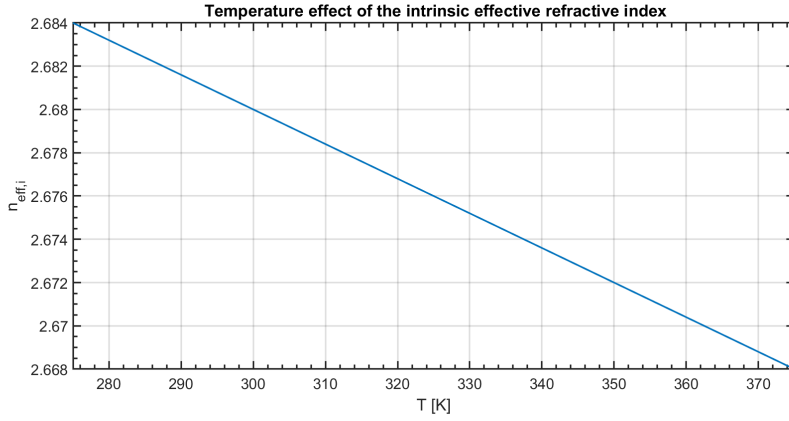
Fig. 2.8 Intrinsic effective refractive index $n_{eff,i}(T)$.

After implementing this temperature effect in the model, it was noticed a significant variation of the T_n characteristic in the resonant wavelength. To highlight the temperature shift, the T_n at different temperatures was plotted on the same graph, and is shown in figure 2.9. Then, it was measured a constant *thermal drift* (TD) of $TD = -80\,pm/K$ ($-0.08\,nm/K$). This value is coherent with results obtained in [21] and with IMEC measurements.
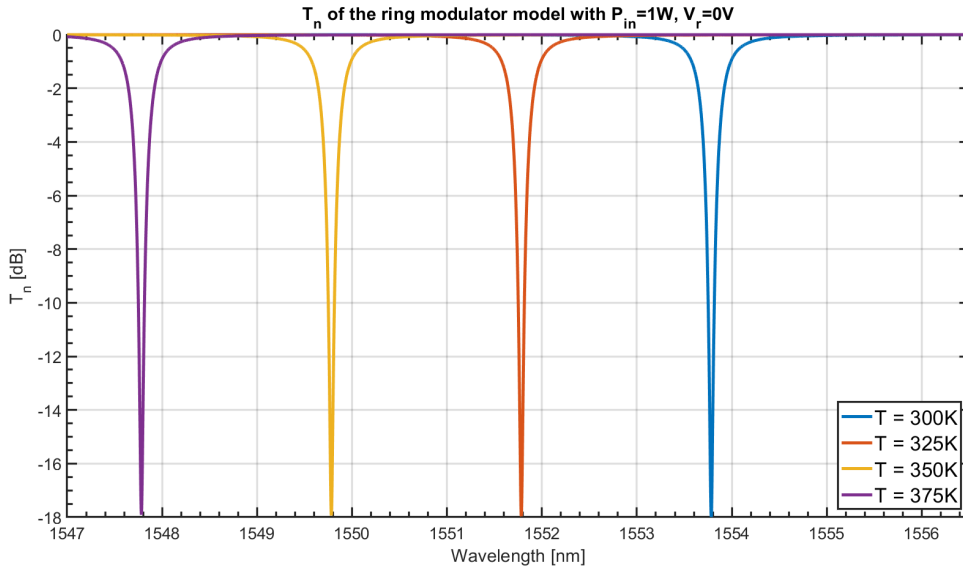
Fig. 2.9 T_n variation of the resonating wavelength at varying the temperature.

2.3 | Fitting of the model with IMEC measurements

In section 2.2.2 it was explained the methodology applied to realized a flexible and valid model, in order to overcome the limitations of the Lumerical Interconnect model presented in section 2.1. The final step, presented in this section, consisted in adjusting the technological parameters, in order to fit the IMEC measurements and to obtain a model behaviour based on a state-of-the-art Si RM.

Firstly, the MATLAB model had to be properly divided in functions, input and output parameters. In fact, in chapter 4 the model built in this chapter will be used as a block for the optical link system.

In fact, up to this point, it was considered the Si RM as a stand-alone system that was wanted to be modeled. However, the Si RM has to be seen and treated as a possible implementation of the optical modulator, which is a block of the optical link system which will be exploited in chapter 4 for a power consumption evaluations.

The modulator is a simple block that receives an input power (P_{in}) and gives an output optical power $P_t = T_n \cdot P_{in}$, depending on the simulation and technology parameters. The simulation parameters are the working condition of the modulator (λ, T, V), while technological parameters are values depending on the technology and the process of realization.

The transfer function T_n was computed with a new-built MATLAB function that evaluates T_n = *transfer_function_RM(tech_param,sim_param)*. The code implemented for this function is available in appendix A.

Subsequently, the second step was to find a combination of the technological parameters, that could best fit the model with the data. A possible approach, could have been to set up a simulation sweep of all the parameters, in order to automatically find the best combination that could fit the measurements. However, this option would have been too much time consuming and it would have been difficult to find a method to select the best combination. For this reason, it was decided to study how each parameter would have affected the microring's characteristics. Moreover, some parameters were set constants, coherently with the IMEC parameters available.

First of all, it was kept a temperature $T_0 = 300\,K$. Then, some of the parameters were fixed to their real physical values, according to the device from which the measurements were obtained. The physical dimensions were set to $R = 5\,\mu m$, $L_j = 500\,nm$. The doping level

concentrations were fixed to $N_A = N_D = 3 \cdot 10^{18} cm^{-3}$. In the end, it was set the group index $n_g = 3.89$ and $n_{eff,i0} = 2.68$ according to IMEC experimental measurements.

The remaining RM technological parameters that could be varied to adjust the model, were:

- the *self-coupling coefficient* (t)

- the *measurement wavelength* (λ_0)

- the *intrinsic absorption coefficient* (α_i)

- the *confinement factor* (γ)

In order to find a good fitting, the most relevant FOMs had to be defined and extracted from the measurements. Since four technological parameters of the RM could be changed, four main spectral characteristics were selected and evaluated on MATLAB: the full width at half-maximum (*FWHM*), the resonating wavelength (λ_r), the drop ($min(T_{n,dB})$) and the modulation efficiency (*ME*). The first two parameters have already been presented. The drop is defined as $min(T_{n,dB}) = T_{n,dB}(\lambda_r)$ and is the minimum value that the v-shape T_n reaches (the value was extracted at 0 V). The modulation efficiency is defined as $ME = \frac{\Delta \lambda_r}{\Delta V}$. This last value was computed between a reverse voltage $V_r = 0\,V$ and $V_r = -2\,V$. The modulation efficiency can be computed as $ME_{[0\,V, -2\,V]} = \frac{\lambda_{r,2\,V} - \lambda_{r,0\,V}}{2\,V}$, expressed in pm/V. These four FOMs described are shown on IMEC measurements in figure 2.10 and their values are summarized in table 2.1.
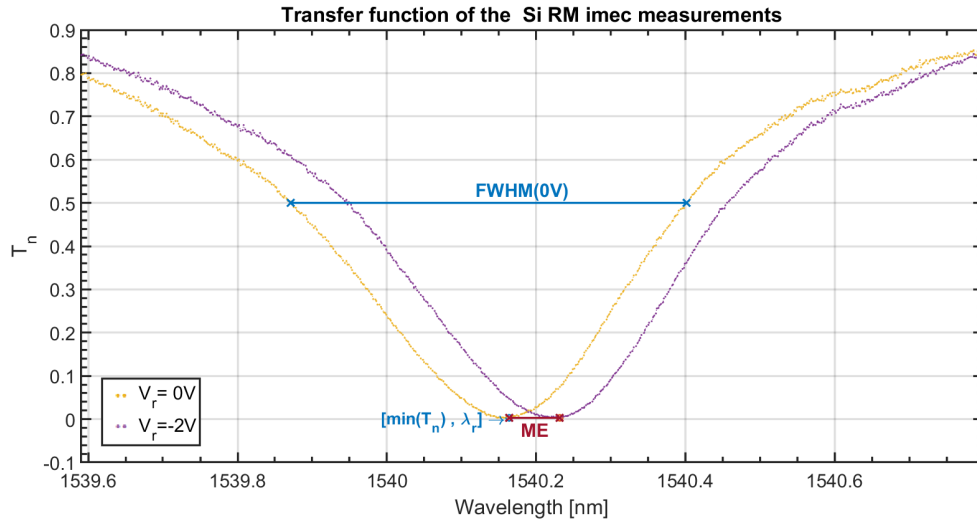
Fig. 2.10 In this figure are represented the four FOMs of interest on IMEC measurements.

After having extrapolated the four FOMs of interest from the data, reported in table 2.1, the next step consisted in the sensitivity study of the four input technological parameters to these four FOMs, in order to properly adjust the model.

Spectral characteristic	Value
$ME_{[0\,V,-2\,V]}[pm/V]$	34.00
$\lambda_{r,0\,V}[nm]$	1540.16
$T_n(0\,V,\lambda_r)[dB]$	-25.2
$FWHM(0\,V)[pm]$	529.8

Table 2.1 Spectral characteristics from IMEC measurements.

2.3.1 | Study of the parameters sensitivity

In order to fit the model with IMEC measurements, a preliminary study was necessary to understand how to adjust the spectral characteristic at its best. The methodology applied for this study was the following. Starting from the same configuration of the parameters presented in the previous section, it was performed a sweep of each one of the four parameters mentioned in 2.3 to evaluate the four FOMs variation. The trend of the four spectral FOMs was plotted for each case and the result of this study is shown in figure 2.11.

21
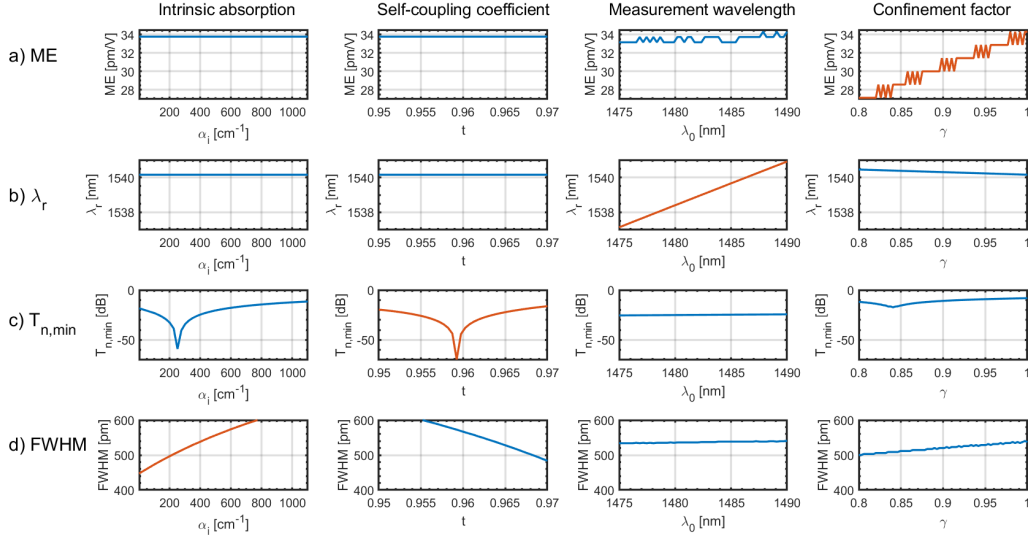
Fig. 2.11 On each line (a)-(d), it has been reported the sensitivity of a specific spectral characteristic with respect to the RM parameters. Moreover, it has been highlighted in orange the parameter that affects the most the spectral characteristic present on the relative line.

From these plots, several interesting properties could be noticed. First of all, the resonating wavelength λ_r and the *ME*, are not affected by variations of the self-coupling coefficient t or the spectral absorption α_i. Moreover, the *ME* doesn't vary significantly with λ_0 variations. The best parameter to adjust the *ME* results then to be the confinement factor γ. Once having set the desired *ME* with γ, the central wavelength λ_r could be adjusted with λ_0, which has a linear dependency with respect to this factor. At this point, since t and α_i don't modify the *ME* and λ_r, these two values could be respectively used to obtain the desired *FWHM* and $P_{t,min}$.

2.3.2 | Choice of the technological parameters for the model

Once having studied in section 2.3.1 how each parameter affected the characteristic, it was easy to adjust the model with respect to the measurements. Firstly, it was varied λ_0, to move the resonating wavelength of the model as close as possible to $\lambda_{r\ imec,0\ V} = 1540.16\ nm$. Then, the *ME* between $0\ V$ and $-2\ V$ was adjusted to the desired value of $34\ pm/V$, by reducing the confinement factor γ. This γ variation increased λ_r and reduced the *FWHM*, as expected from the previous study. For this reason, the λ_0 was varied again to bring the characteristic back to the desired λ_r. Then, the absorption α_i was changed to obtain $FWHM(0\ V) = 529.8\ nm$. In the end, the self-coupling coefficient t was modified to obtain

$T_{n,dB}(0\,V, \lambda_r) = -25.2\,dB.$

Parameter	$\lambda_0[nm]$	$n_{eff,i}$	$\alpha_i[m^{-1}]$	$T = T_0[K]$	γ
Value	1566.1	2.68	270	300	0.995
Parameter	$N_A = N_D[cm^{-3}]$	n_g	$L_j[nm]$	$R[\mu m]$	t
Value	$3 \cdot 10^{18}$	3.98	500	5	0.9557

Table 2.2 Si RM technology parameters set in the model to fit IMEC measurements.

The simulation performed with the set of parameters summarized in table 2.2, is shown in figure 2.12. In the same plot have been displayed also the T_n IMEC measurements that wanted to be matched, both in dB units, as $T_{n,dB} = 10\log_{10}(T_n)$.
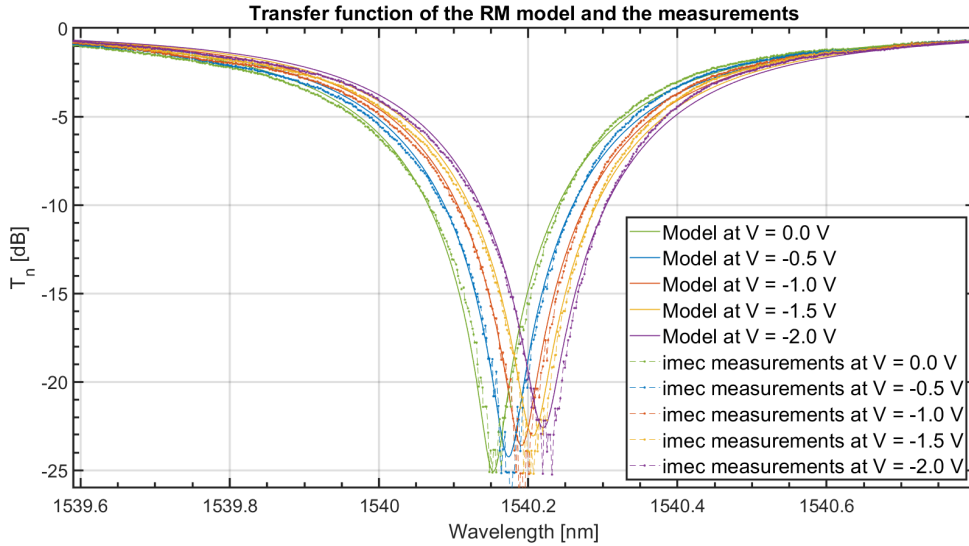
Fig. 2.12 Comparison between the IMEC measurements and the model with the parameters set in tab. 2.2

2.3.3 | FOMs and spectral characteristics of the fitting model

The final step of this chapter, after having built a properly-fitting model, consisted in extracting all the relevant FOMs and spectral characteristics. With the same script used in the previous sections, the spectral characteristics of the model were carried out. The results are summarized in table 2.3.

Spectral characteristic	IMEC measurements	Fitting model
$ME_{[0\,V,-2\,V]}[pm/V]$	34.00	33.5
$\lambda_{r,0\,V}[nm]$	1540.16	1540.154
$T_n(0\,V, \lambda_r)[dB]$	-25.2	-25.1
$FWHM(0\,V)[pm]$	529.8	529.7

Table 2.3 Comparison of the spectral characteristics of the IMEC data and the fitting model.

In the end, the *OMA*, the *ER* and the *IL* were extracted with the same formulas described in section 2.1.1, re-using the script already implemented. In order to compare the model obtained, the *OMA* was plotted on the same graph to compare it with the measurements. The result of the plots is visible in figures 2.13 and 2.14.
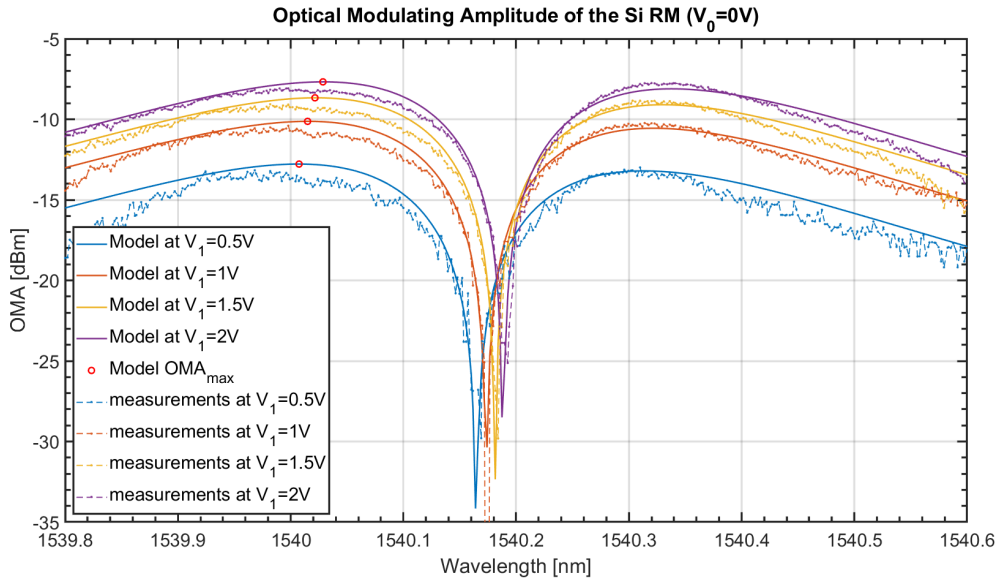
Fig. 2.13 Comparison between the *OMA*[*dBm*] computed from the model and the measurements.
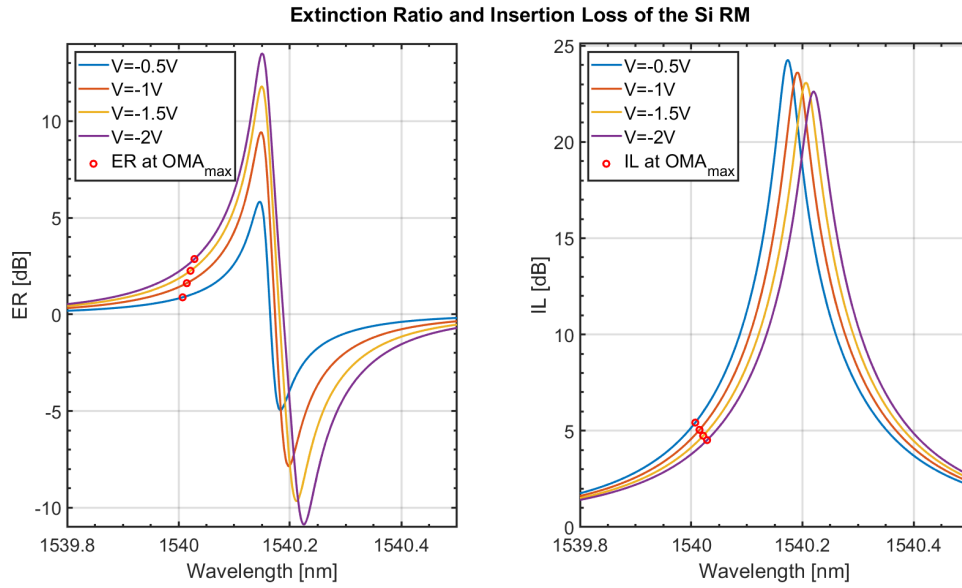
Fig. 2.14 $ER[dB]$ and $IL[dB]$ obtained from the MATLAB model built.

To conclude the study performed in this chapter, the FOMs relative to the optimum case of maximum OMA were evaluated and are summarized in table 2.4.

measurements FOMs					
$V_r[V]$	$\lambda_{pk}[nm]$	$OMA_{max}[dBm]$	$ER_{@OMA_{max}}[dB]$	$IL_{@OMA_{max}}[dB]$	$TP_{min}[dB]$
-0.50	1539.968	-13.16	0.62	5.06	16.17
-1.00	1539.998	-10.40	1.37	5.37	13.41
-1.50	1539.982	-9.07	1.60	4.36	12.08
-2.00	1539.998	-8.08	2.13	4.33	11.09
Model FOMs					
$V_r[V]$	$\lambda_{pk}[nm]$	$OMA_{max}[dBm]$	$ER_{@OMA_{max}}[dB]$	$IL_{@OMA_{max}}[dB]$	$TP_{min}[dB]$
-0.50	1540.007	-12.78	0.88	6.31	15.79
-1.00	1540.015	-10.13	1.61	5.71	13.14
-1.50	1540.022	-8.67	2.25	5.28	11.68
-2.00	1540.029	-7.68	2.86	4.97	10.69

Table 2.4 Results of the main FOMs from the model fit and the IMEC data.

3 Electro absorption modulator

An electro absorption modulator is a different type of optical modulator, which is based on the *electro-absorption effect.* There are two different electro-absorption effects in semiconductors: the Franz-Keldysh effect (FK) and the Quantum Confined Stark Effect (QCSE). In this chapter it will be presented the modeling of a FK Electro Absorption Modulator (FK-EAM) in $Ge_{1-x}Si_x$ with $x = 0.8\%$ [10],[22]. Germanium (Ge) is an interesting material for high performances MOSFETs [23], but it works at higher wavelengths ($\sim 1.65 \ \mu m$) with respect to the c-band. For this reason, a lot of progresses on growing Ge on Si have been obtained in the last years [24]. In this section it will be studied the modeling of the GeSi FK-EAM, applying the same methodology steps presented in chapter 2.

3.1 | The Franz-Keldysh effect

The physical effect of the FK-EAM modulator that is going to be presented in this chapter is the Franz-Keldysh effect (FK). The variation of the absorption coefficient for the direct band gap due to the FK is well expressed in the book [25], as:

$$\alpha = \alpha_{direct}(\hbar\omega, F) = \frac{A_0}{2\pi} \left(\frac{2m_r^*}{\hbar^2} \right)^{3/2} \cdot \sqrt{\hbar\theta_F} \left(-\eta A_i^2(\eta) + A_i'^{\,2}(\eta) \right)$$

$$where \quad \eta = \frac{E_g - \hbar\omega}{\hbar\theta_F} \ , \qquad \hbar\theta_F = \left(\frac{\hbar^2 q^2 F^2}{2m_r^*} \right)^{1/3} \quad and \quad A_0 = \frac{2\pi\hbar q^2 \cdot E_{MM}}{\sqrt{\varepsilon_r \varepsilon_0} \cdot c \cdot m_0 \cdot E_{ph}}$$

In the formulas mentioned right above, $q = 1.6 \cdot 10^{-19} \ C$ is the electron charge, $\varepsilon_0 = 8.86 \cdot 10^{-12} \ \frac{F}{m}$ is the dielectric constant, $m_0 = 9.109 \cdot 10^{-31} \ kg$ is the electron rest mass, $c = 3 \cdot 10^8 \ m/s$ is the speed of light in vacuum, $h = 6.626 \cdot 10^{-34}$ is the Plank constant and $\hbar = \frac{h}{2\pi}$.

Moreover, $E_{g,eV}(T) = E_{g,eV}(0\,K) - (4.8 \cdot 10^{-4}\frac{eV}{K} \cdot T^2)/(T + 235)$ is the energy gap in [eV] depending on the temperature T. To be applied in the formula, this value has to be converted in J $E_g = E_{g,eV} \cdot q$, $m_r^* = m_r \cdot m_0$ is the effective mass with m_r a constant that depends on the material and $E_{MM} = 23q$.

The applied field F, could just be computed with respect to the applied peak-to-peak voltage on the FK-EAM as:

$$F = \frac{V}{d}, \text{ where d is the physical dimension of the FK-EAM}$$

Moreover, $A_i(\eta)$ and $A_i'^2(\eta)$ are the *Airy function* A(x) and its primitive derivative, which can be computed with the MATLAB function *airy(K,X)* [26].

An important relation to remember is the one between the photon energy (E_{ph}) and the wavelength (λ), which is:

$$E_{ph} = \hbar\omega = \frac{c \cdot h}{\lambda}$$

Since the same problems already described in chapter 2 would be experienced in using Lumerical Interconnect, it was directly proceeded to build a MATLAB FK-EAM model.

3.2 | GeSi FK-EAM modeling

A good strategy to start to study how to model the FK-EAM, was to begin from presenting its transfer function T_n, which can be computed as:

$$P_{out} = P_{in} \cdot e^{-\alpha L} \quad \rightarrow \quad T_n = e^{-\alpha L}$$

where α was the absorption of the material, P_{in} is the optical input power to the modulator and L is the length of the device.

Then, the second step was to understand which parameters depend on the wavelength and applied field, since the final goal is to obtain $T_n = T_n(\lambda, V)$. For a FK-EAM, the only parameter that can have a dependency is the absorption coefficient due to the FK effect.

Due to its structure, the GeSi FK-EAM is supposed to have an indirect band gap diagram. However, as expressed in 3.1, a well known formula for the FK direct band gap devices, expressed in the book [25], is:

$$\alpha = \alpha_{direct}(\hbar\omega, F) = \frac{A_0}{2\pi} \left(\frac{2m_r^*}{\hbar^2} \right)^{3/2} \cdot \sqrt{\hbar\theta_F} \left(-\eta A_i^2(\eta) + A_i'^{\,2}(\eta) \right)$$

The final goal of this study was to obtain a suitable model for the FK-EAM modulator. The idea was to use the formula for the direct band gap and to adjust the parameters to fit the state-of-the-art data, as done in chapter 2. The first step was then to obtain a working model for the pure Ge FK-EAM, by setting the physical parameters of the Germanium provided by the *Ioeffe Institute*[27].

The obtained absorption coefficient with the parameters set is shown in figure 3.1. For this simulation, there were applied three different voltages $V = [0, -1, -2]$ V, to notice the FK effect on the absorption coefficient. On the left side of figure 3.1 is shown the absorption coefficient α of Ge vs photon energy (E_{ph}) at 300 K for different fields. On the right side of the same figure is shown the plot of the absorption coefficient vs wavelength ($\lambda = c \cdot h / E_{ph}$) under the same conditions.
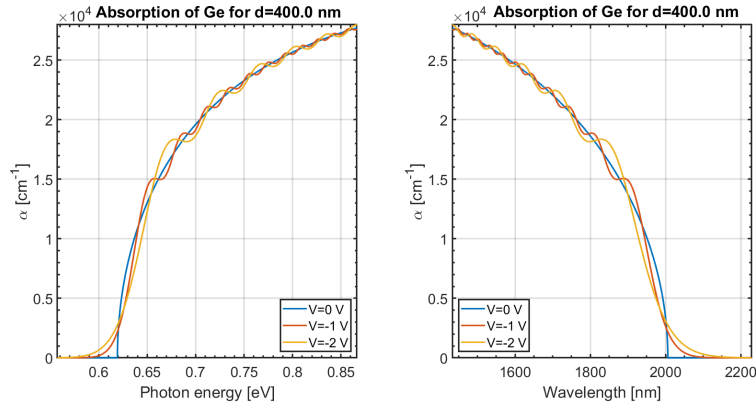
Fig. 3.1 Absorption coefficient of the FK-EAM in Germanium for different voltages.

After this step, the MATLAB code was divided in functions as previously done for the Si RM, in order to use it as an alternative "piece" for what concerns the optical modulator in the optical link system power evaluation. The MATLAB function built for evaluating the T_n transfer function is reported in appendix B.1.

3.2.1 | Fitting the FK-EAM model with measurements

Once having studied the parameters dependencies, the parameters were varied to fit the IMEC data with the same procedure applied in the previous chapter. In particular, the energy gap was changed to align the characteristic between the model and the measurement (shift on the wavelength axis). Then, the m_r^* was slightly changed to fit the data.

The final set of parameters used to the fitting model of the FK-EAM is summarized in table 3.1.

Parameter	$E_{g,0K}[eV]$	$d[nm]$	$L[\mu m]$	m_r^*/m_0
Value	0.886	500	40	0.035

Table 3.1 FK-EAM technology parameters set in the model to fit the IMEC data.

The implemented *GeSi* FK-EAM transfer function model ($T_n = e^{-\alpha L}$) is shown in figure 3.2 for an applied voltage $V_{pp} = [0,1,2,3] \, V$. On the same plots, it has been superimposed the IMEC measurements obtained for $V_{pp} = [0,1,2] \, V$.
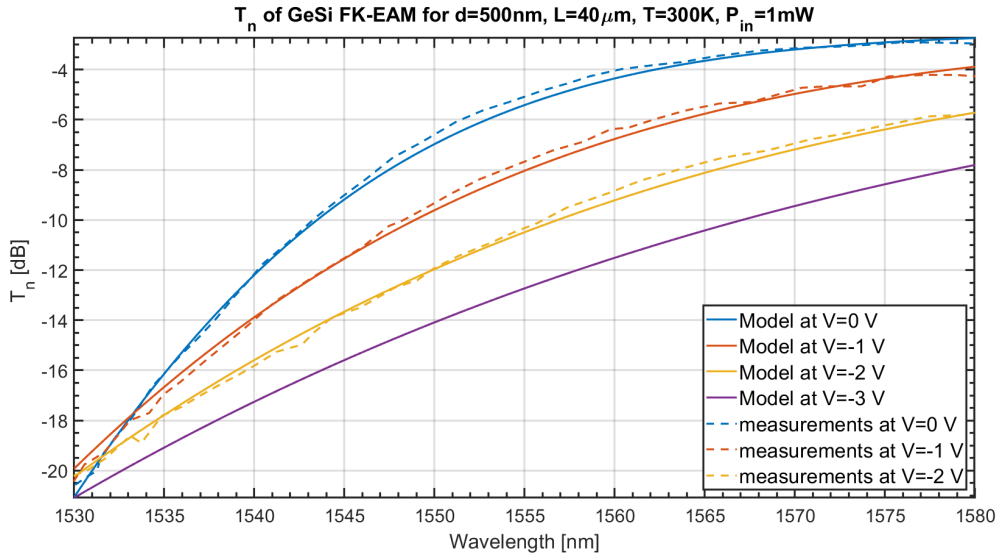
Fig. 3.2 Absorption coefficient α of Ge vs wavelength at 300 K for different fields.

3.2.2 | FOMs of the FK-EAM model

Once having obtained and adjusted the model with the measurements, the extraction of the most interesting FOMs was performed as done for the Si RM. In particular, it was evaluated

the $OMA[dBm]$, the $ER[dB]$ and the $IL[dB]$ for $V_{pp} = [1, 2, 3]\ V$, with the same formulas presented in 2.

The result of this evaluation is shown in figures 3.3 and 3.4. The values obtained with the model built are coherent with other studies, such as in [28].
Unfortunately, the measurements for the FK-EAM at different voltages, were provided at different wavelengths, so it could not be performed the FOMs study for the measurements.
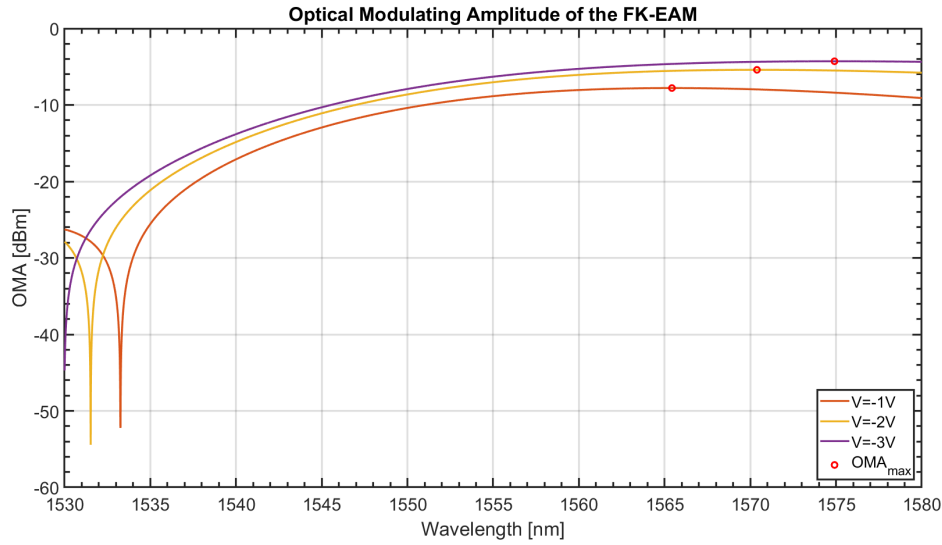
Fig. 3.3 OMA of the FK-EAM model.

Moreover, as done in chapter 2, a summary of the values of all the FOMs obtained at the OMA_{max} condition is reported in table 3.2.

FK-EAM model FOMs					
$V_r[V]$	$\lambda_{pk}[nm]$	$OMA_{max}[dBm]$	$ER_{@OMA_{max}}[dB]$	$IL_{@OMA_{max}}[dB]$	$TP_{min}[dB]$
-1.00	1565.43	-7.79	2.08	5.69	10.80
-2.00	1570.39	-5.41	3.95	7.12	8.42
-3.00	1574.91	-4.29	5.67	8.59	7.30

Table 3.2 Results of the main FOMs from the FK-EAM model at OMA_{max} condition.
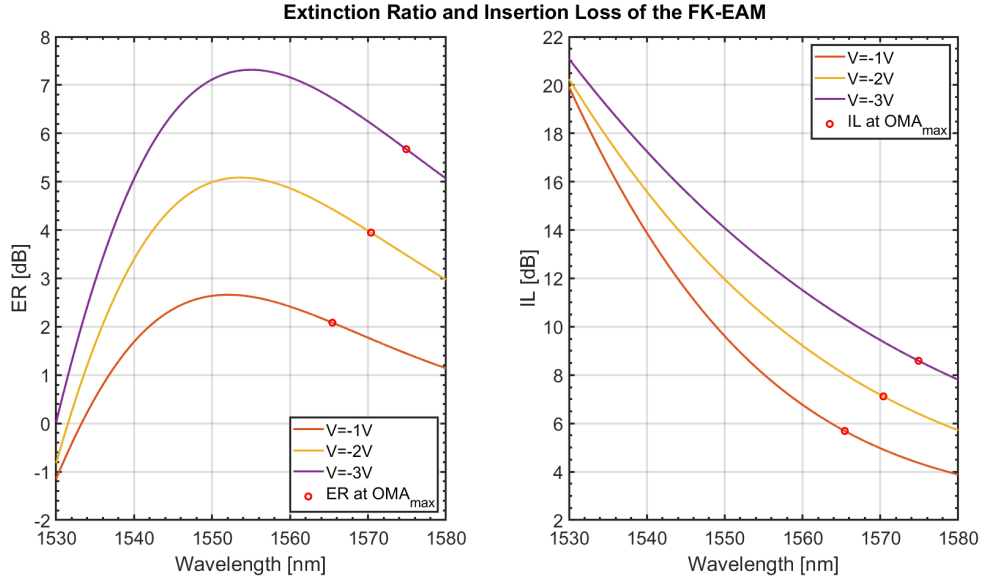
Fig. 3.4 ER and IL for the FK-EAM model.

What is interesting to notice is that, with respect to the Si RM, the FK-EAM has a counter-effect on the performances. By increasing the voltage, the *ER* increases, however the *IL* increases also.

3.2.3 | Temperature dependency of the FK-EAM

The last interesting study for this chapter, as already done for the Si RM and for the same reasons, is the study of the temperature dependency of the transfer function. The only parameter that depends on the temperature and that significantly shifts the characteristic is the energy gap:

$$E_{g,eV}(T) = E_{g,eV}(0K) - \frac{4.8 \cdot 10^{-4} \frac{eV}{K} \cdot T^2}{T + 235}$$

In figure 3.5 is shown the temperature shift for $T = [300, 325, 350]\,K$. From the plot it was computed a shift of 18.9 *nm* from $T = 300\,K$ to $T = 325\,K$, and a shift of 19.5 *nm* from $T = 300\,K$ to $T = 350\,K$. This means that the temperature shift experienced is 760 *pm/K* in one case and of 780 *pm/K* in another case.
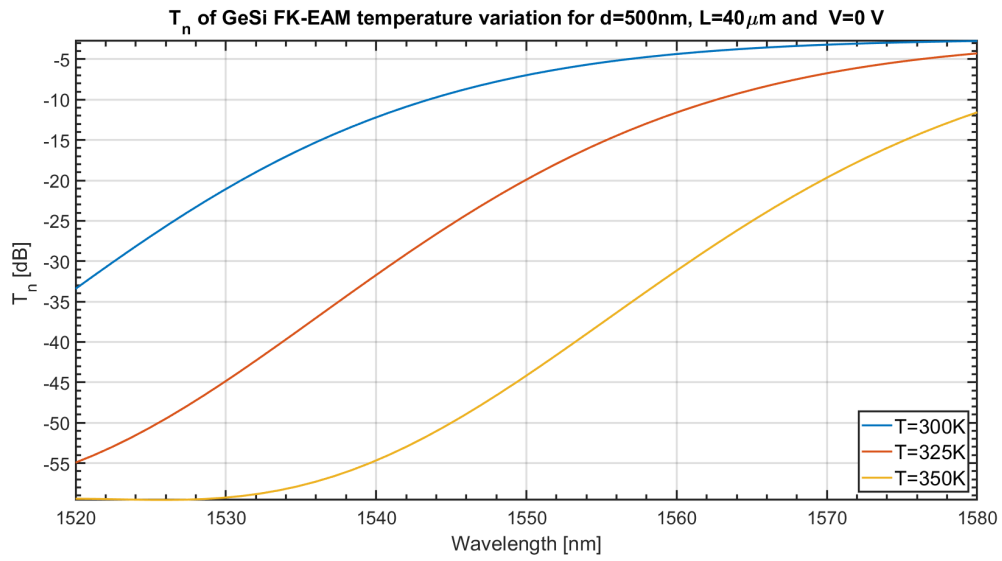
Fig. 3.5 $T_{n,dB}$ of the FK-EAM at $V = 0\,V$, at different the temperatures.

It can be noticed that the FK-EAM transfer function shifts to the right by $TD = +0.78\,nm/K$, while the Si RM was shifting to the left by $TD = -0.08\,nm/K$. This means that the FK-EAM is 10 times more sensitive to temperature with respect to the Si RM.

4 Optical link system

Once having obtained the models for the two optical modulators, the final step was to exploit these models in an already-existing framework for simulating the optical link performances and power consumption. Then, before starting to make this comparison, the different blocks of the simulation have to be presented.

As already expressed in chapter 1, the optical link system block diagram is shown in figure 4.1. In this figure have been added some components that were not presented in the introduction chapter. Moreover, also some figures of merit have been reported on the schematic block.
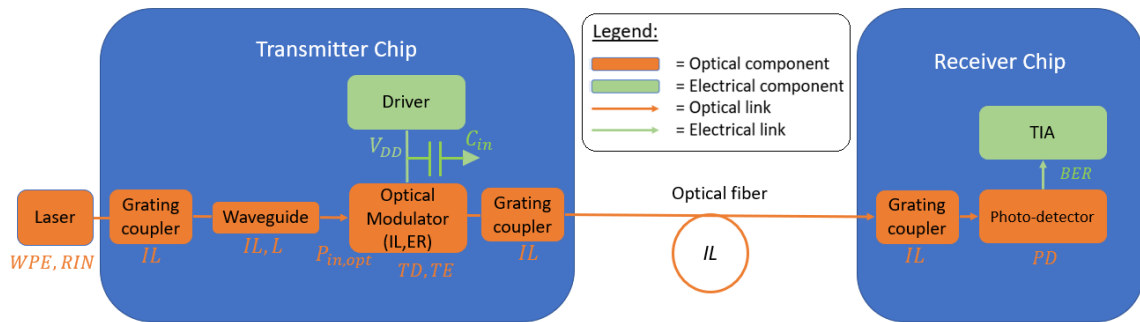
Fig. 4.1 The optical link system blocks included the already-existing simulation.

The optical link system is divided in two parts: the transmitter and the receiver side. The already-existing simulation starts its analysis from the receiver, and goes back to the transmitter in order to reverse-compute the parameters desired. At the receiver is set the desired bit error rate ($BER = 10^{-12}$). From the BER, the *OMA* needed for reaching this minimum bit error rate was computed according to [29].

On the transmitter side, some grating couplers have been considered to guide the light from a waveguide to another between two different devices, as well as for the receiver. The first block of the transmitter is the laser. Its most important figure of merit is the wall-plug efficiency, which is the ratio between the generated optical power and the electrical power consumed by the laser ($WPE = P_{opt}/P_{el} = 10\%$). Moreover, it was also considered the relative intensity noise ($RIN = -140\,dBc/Hz$) of the laser. The optical power is then coupled through a waveguide, which couples the light in the optical modulator. The modulator is driven by an electrical driver, which consumes a driving power proportional to the input capacitance of the modulator $P_{drive} = C_{drive}V_{DD}^2$. Moreover, in the simulation is also taken into account the temperature effect on the two optical modulators, considering their thermal efficiency (TE) and thermal drift (TD), and supposing a temperature variation of $25\,K$. Between the two sides, it was considered an optical fiber of a length $L = 2\,km$, thus a loss of $2\,dB$.

At the receiver, the optical power is converted with a photo-diode into a current, with a *responsivity* factor R. The *transimpedance amplifier* is the last block of the receiver and is an electrical component that converts the current into a voltage (TIA was optimized and modeled as an inverter with a feedback resistor using an already-existing script).

4.1 | Si RM and FK-EAM energy consumption

The aim of this chapter was then to exploit the two models of the optical modulator, in order to evaluate which technology optimizes the energy consumption per bit of the optical link system. Both models of the modulators can be used in the simulation for the optical modulator block. This chapter will try to understand if there is a modulator that is "better" from a power consumption point of view and why/why not. The simulation parameters presented in section before, are then reported in table 4.1. For both optical modulators, it was simulated a driving voltage of $V_1 = [1,2]V$. Moreover, in the simulation it was set a limit to the optical input power into the modulator $P_{in,opt} = 1mW$ ($P_{in,dBm} = 0dBm$). This limitation is for two main reasons: because a too high input powers generates self-heating that is not considered and because a too high input power modifies the transfer function in a non-linear way. Since the models implemented do not consider this non-linear regime, the models are not valid for input optical power higher than 1mW and thus are discarded from the simulation.

An important parameter to notice is the $\Delta\lambda$. This parameter is the wavelength shift that has to be applied to the modulator with an heater. In this temperature shift, two phenomena are considered: process variation and temperature variation. For the Si RM, the process variation

is considered to be 2 *nm*, to which other 2 *nm* are added to consider the chip temperature variation ($\frac{2\,nm}{0.08\,nm/K} \sim 25\,K$). From this value, 0.15 *nm* which correspond to the half of the *1dB optical bandwidth* of the *OMA* are then subtracted. This is because by moving of that wavelength shift, the *OMA* performances degrade of less than 1dB. The shift was then set to $\Delta\lambda_{RM} = 2\,nm + 2\,nm - 0.15\,nm = 3.85\,nm$. Since the FK-EAM is 10 times more sensitive to temperature variations with respect to the Si RM, a wavelength shift of $\lambda = 20\,nm$ should be considered for the temperature variation of 25 *K*. However, the 1dB optical bandwidth of an FK-EAM is approximately 30 *nm* (from fig. 3.3). For this reason, 15 *nm* can be removed and it can be considered the $\Delta\lambda_{EAM} = 20\,nm + 2\,nm - 15\,nm = 7\,nm$.

Component	Parameter	Value	Component	Parameter	Value
Laser	WPE	10%	Fiber	IL	$2\,dB$
	RIN	$-140\,dB/Hz$	Photodiode	R	$0.8\,A/W$
Grating coupler	IL	$2\,dB$	TIA	V_{swing}	$0.8\,V$
Waveguide	IL	$1dB$	Receiver	BER	10^{-12}
	Length	$3\,mm$			
		Optical Modulator			
Si RM	IL, ER	from models	FK-EAM	IL, ER	from models
	C_{in}	$55\,fF$		C_{in}	$55\,fF$
	TD	$0.08\,nm/K$		TD	$0.8\,nm/K$
	TE	$3.75\,mW/K$		TE	$1\,mW/K$
	$\Delta\lambda$	$3.85\,nm$		$\Delta\lambda$	$7\,nm$

Table 4.1 Parameters set for the simulation of the optical link system.

4.1.1 | Energy consumption of the Si RM

After having set the simulation parameters as shown in table 4.1, the simulation was performed starting from the Si RM model. The result is reported in figure 4.2. The picture shows each component of the energy per bit dissipation ($E_{bit} = P \cdot f_{bitrate}$). All the different components of power consumption are stacked on an histogram, to visualize the total energy consumption per bit at each bit rate. It can be noticed from figure 4.2 (left) that after $f_{bitrate} = 20\,Gbps$ the histogram does not continue. The reason is because it was limited the maximum input power to the modulator to 0 *dBm*, because for higher values the modulator suffers of non-linearities and self-heating effects and thus the implemented models are not

valid any more. This means that the Si RM with an applied voltage $V_1 = 1\ V$ is limited to work at 20 *Gbps*, according to the provided model. This statement is kept valid during all the paper.
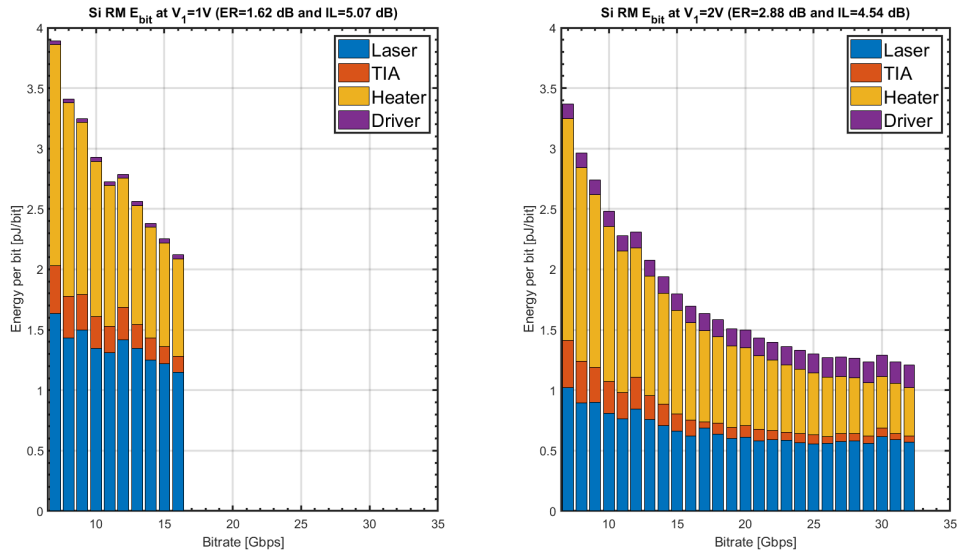
Fig. 4.2 Optical link system energy consumption per bit with Si RM.

4.1.2 | Energy consumption of the FK-EAM

The same procedure described in 4.1.1 was repeated, substituting the Si RM with the FK-EAM. The result is displayed in figure 4.3. It can be immediately noticed that the power consumption of the FK-EAM is lower than the previous case for both 1 V and 2 V. In chapter 6 the results will be compared and analysed.
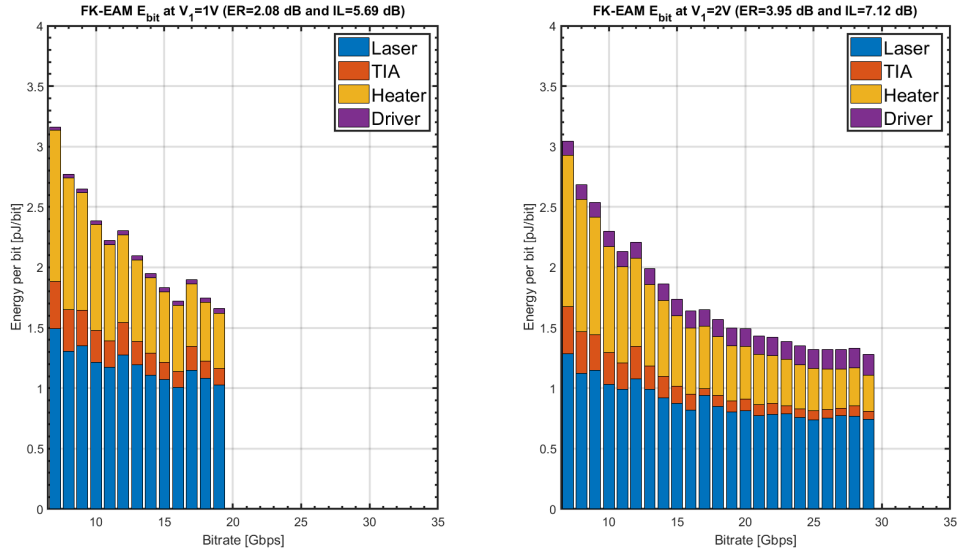
Fig. 4.3 Optical link system energy consumption per bit with FK-EAM.

4.2 | Considering only 25 K of temperature variations

The steps described in section 4.1 were referring to the analysis of temperature variations for both process variation compensation and room temperature. In this section and in section 4.3, it will be presented the study of the two single cases, as clearly expressed in the section titles.

As done for the previous case, the optical link system parameters were set according to the state-of-the-art values. The only parameter that was changed was the wavelength shift $\Delta\lambda$ that was set for considering 25 K of variation.

Thus, for the $\Delta\lambda_{RM} = 2\,nm - 0.15\,nm = 1.85\,nm$ and for the $\Delta\lambda_{EAM} = 20\,nm - 15\,nm = 5\,nm$. The results of the simulation performed for the two devices at $V = [1,2]\,V$ under the conditions specified above are visible in figure 4.4.
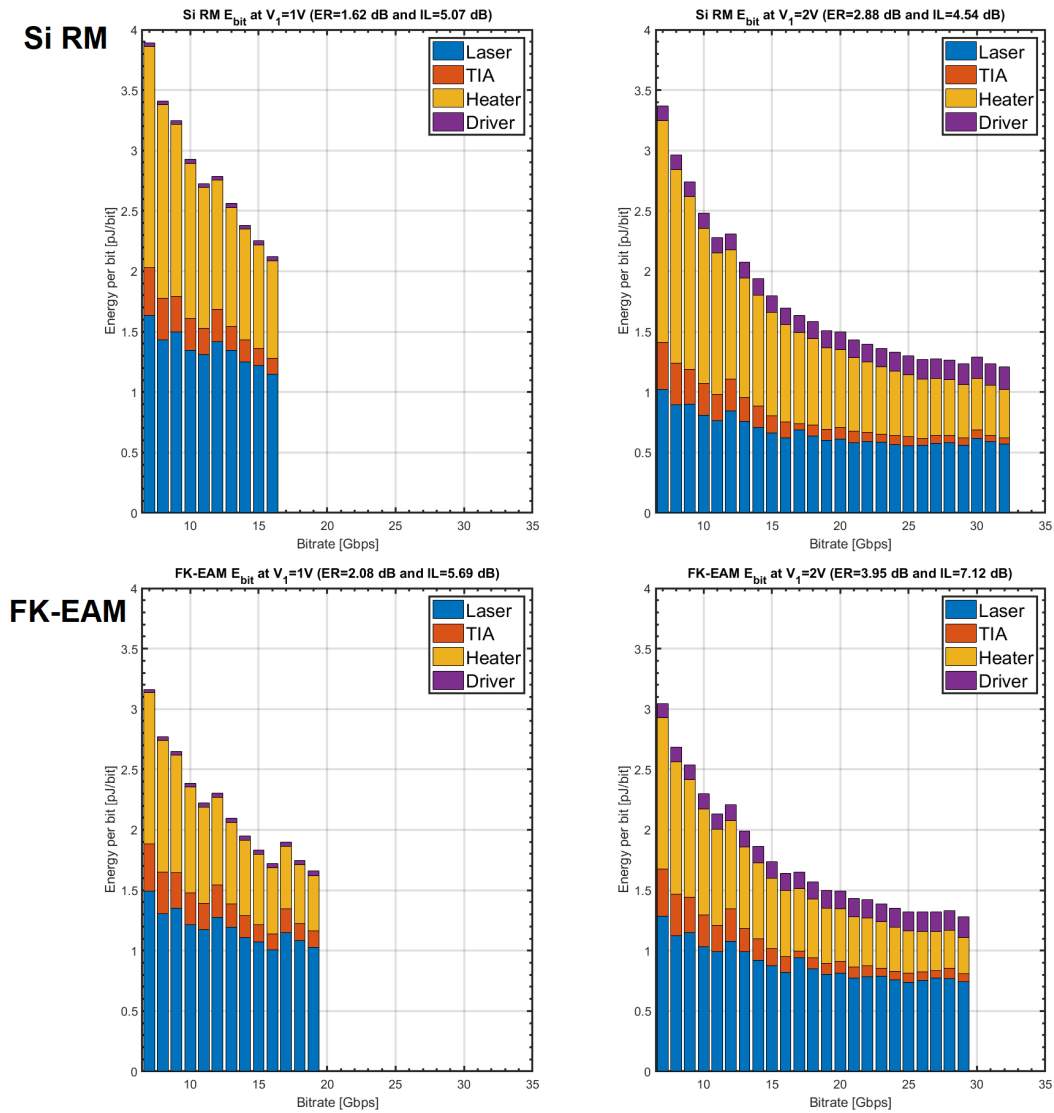
Fig. 4.4 Optical link system energy consumption per bit with Si RM and FK-EAM under several applied voltages and considering only the room temperature variation.

4.3 | Considering only process variations

Also in this case, the methodology strategy was the same. All the optical system parameters were kept unchanged and the only parameter that was changed was the wavelength shift, in order to consider 2 nm of process variation for both devices.

Thus, for the $\Delta\lambda_{RM} = 2\,nm - 0.15\,nm = 1.85\,nm$. For the FK-EAM the computation should be $\Delta\lambda_{EAM} = 2\,nm - 15\,nm = -13\,nm$, however a negative temperature shift simply means that for the FK-EAM it is not necessary to tune the device for adjusting process variation, so the shift can be set to $\Delta\lambda_{EAM} = 0\,nm$.

The results of the simulation performed for the two devices at $V = [1, 2]\,V$ under the conditions specified above are visible in figure 4.5.
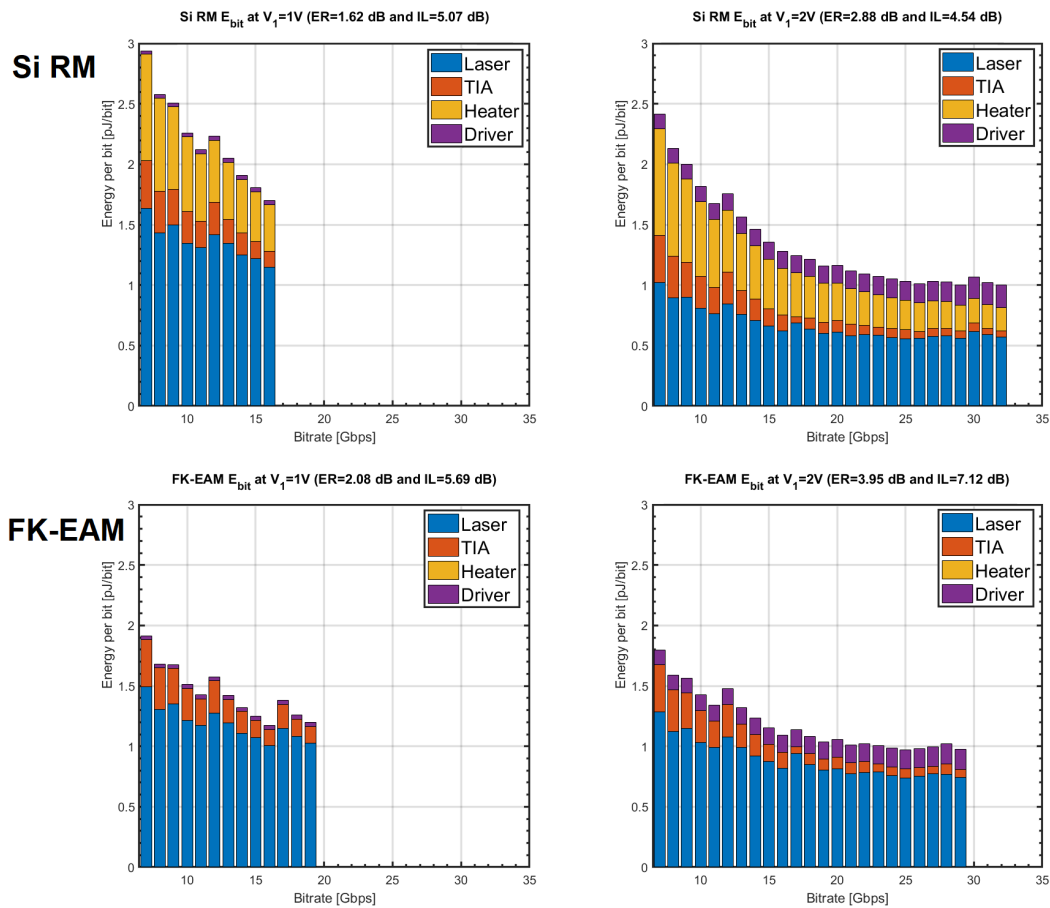
Fig. 4.5 Optical link system energy consumption per bit with Si RM and FK-EAM under several applied voltages and considering only the process variation.

5 Results and discussion

5.1 | Silicon ring modulator

The aim of the study performed in chapter 2 was to obtain a sufficiently flexible model, that allows the possibility to adjust the simulation parameters for fitting experimental measurements.

It can be clearly stated that the model built allows a large flexibility, allowing to simulate the behaviour of a Si RM in different technological parameters set and at various conditions. In particular, the desired flexibility for temperature was achieved since a temperature variation affects the model as expected from measurement data. The obtained variation of -80 pm/K of the resonating wavelength, is coherent with the experimental values measured in different experiments. This temperature shift is due to the factor $\frac{\partial n_{eff}}{\partial T} = 2.05 \cdot 10^{-4} \ K^{-1}$; thus, it is just necessary to change this value to adjust the temperature variation if needed.

About the accuracy of the model fitting with the IMEC measurements, it can be affirmed that the model parameters were properly set to fit the model. The relative errors of the model approximation could be computed as:

$$\varepsilon_{r,\%}(V) = \left| 100 \cdot \frac{P_{t,model}(V) - P_{t,imec}(V)}{P_{t,imec}(V)} \right|$$

By applying this formula to the values shown in figure 2.12, the result was that the average error was around 5.2%. This was expected, since the measurement data show a non-ideal behaviour around λ_r. Moreover, as already mentioned, the optimum working condition of the ring modulator is at the OMA_{max}. In the working area of the OMA_{max} ($\lambda \sim 1540 \ nm$), the model fits sufficiently well the measurements.

5.1.1 | Flexibility of the model

As asserted multiple times, the goal of this section was to obtain a model which allowed an adaptability in the temperature dependency. However, in section 2.3, the fitting was realized keeping some parameters constants and changing just some of them. The study performed in 2.3.1 could be extended to all the technology parameters, in order to have a wider range of parameters available to fit the data. An example is presented.

Starting from a different doping concentration $N_A = N_D = 4 \cdot 10^{18} cm^{-3}$ and applying the same methodology described in 2.3.2, the parameters were changed to a different set, shown in table 5.1.

Parameter	$\lambda_0[nm]$	$n_{eff,i}$	$\alpha_i[m^{-1}]$	$T = T_0[K]$	γ
Value	1505.03	2.68	20	300	1
Parameter	$N_A = N_D[cm^{-3}]$	n_g	$L_j[nm]$	$R[\mu m]$	t
Value	$4 \cdot 10^{18}$	3.98	500	5	0.9556

Table 5.1 A different configuration of the Si RM technology parameters set to fit the data.

The result of these parameters change is shown in figure 5.1. As it has been shown, the parameters can be adjusted to fit the data also in a different configuration and this proofs the flexibility of the model.
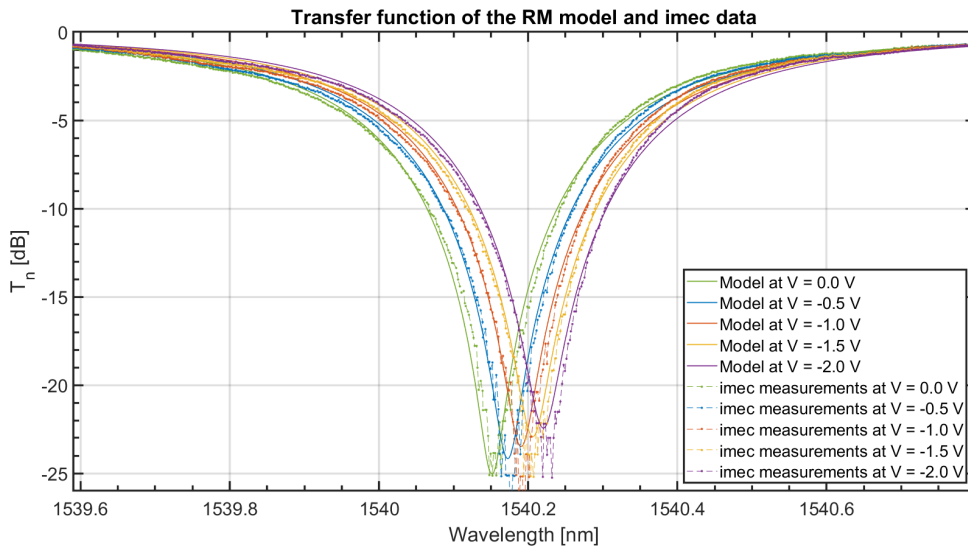
Fig. 5.1 Comparison between the IMEC data and the model with a different set of parameters, in particular under different doping concentrations with respect to figure 2.12.

Nevertheless, it is important to highlight that, even if in both cases a good model could be obtained, not in both cases the parameters set have a physical meaning. For example, the confinement factor $\gamma = \frac{P_{core}}{P_{tot}} \in [0,1]$, assumes the value 1 just in a theoretical way, since there will always be a tail of the optical field going out from the core. In the same way, an intrinsic absorption $\alpha_i = 20\ m^{-1}$, is not coherent with the typical expected values at $\lambda_0 = 1505.03\ nm$. However, if the goal is the implementation of a model that follows the measurements, this model can help to obtain the goal.

5.2 | GeSi FK-EAM

As done in section 5.1, the relative error was computed for the three different voltages as $\varepsilon_{r,\%}(V) = \left| 100 \cdot \frac{T_{n,model}(V) - T_{n,imec}(V)}{T_{n,imec}(V)} \right|$. In order to evaluate this value, the $T_{n,model}(V)$ had to be computed at the same wavelengths of the IMEC data, in order to be able to compute the difference between the model and the data. Then, once having evaluated the relative error for three different applied fields/voltages ($V = [0, -1, -2]\ V$), the *standard deviation* for each voltage was computed, in order to compute the average error ($\overline{\varepsilon_{r,\%}}$) as the arithmetic mean:

$$\sigma(V) = \sqrt{var(\varepsilon_{r,\%}(V))} \rightarrow \overline{\varepsilon_{r,\%}} = \frac{\sigma(0\ V) + \sigma(-1\ V) + \sigma(-2\ V)}{3}$$

The obtained average error of the model was computed to be $\overline{\varepsilon_{r,\%}} = 3.2\%$.

Also in this case, the model has a large flexibility that allows the user to set the correct parameters to fit the experimental data and also to adjust the temperature effect.

5.3 | Optical link system

Some simulations of the energy consumption per bits have been presented in Chapter 4. From figures 4.2 and 4.3 it can be clearly stated that in the cases studied there is no device that shows better performances that the other, and the performances change a lot with respect to the simulated temperature and process variation conditions. The main reason is because, even if the FK-EAM has higher insertion losses than the Si RM, it also has much higher extinction ratio; the FK-EAM is also less sensitive to process variations thanks to its high 1dB bandwidth but it is more sensitive to temperature. Moreover, the heater is one of the main sources of consumption in both cases ($\sim 30\%$) when considering all the variations together. The heater energy consumption per bit decreases by increasing the $f_{bitrate}$, because the power of the heater is constant, thus $E_{bit,heater} = P_{heater}/f_{bitrate}$. The same consideration is valid for the TIA consumption. About the laser power consumption, it is interesting to

notice that for the Si RM, the energy per bit decreases while increasing the driving voltage. This is because the IL decreases and the ER increases. On the other hand, for the FK-EAM the laser energy consumption per bit keeps constant. This is because the ER increases by increasing the driver voltage, but also the insertion loss increases. The heater of the Si RM is more difficult to realize and has a large area, thus it occupies more chip area. There are lots of considerations that have to be done and there is no evidence for preferring one device to the other. The aim of this master thesis work was only to provide models for future and more accurate optical link analysis and this result was reached.

6 Conclusion

The aim of this master thesis was to built models of optical modulators for allowing optical link analysis, since no models were available in the IMEC framework. After having performed a study on the physics behind two different modulator technologies, the two desired models were successfully built and fitted with IMEC measurements, in order to obtain models that were behaving as state-of-the-art devices.

Subsequently, it was possible to include the two implemented models to perform some power consumption analysis of the optical link system. From figure 6.1, it is evident that the FK-EAM and Si RM at 2 V have analogue performances for what concerns the energy consumption. The FK-EAM performances at 1 V are slightly worse than the case of FK-EAM at 2 V, but not significantly. The Si RM at 1V resulted to have worse energy consumption per bit with respect to the other cases, with a $\sim 30\%$ higher consumption.
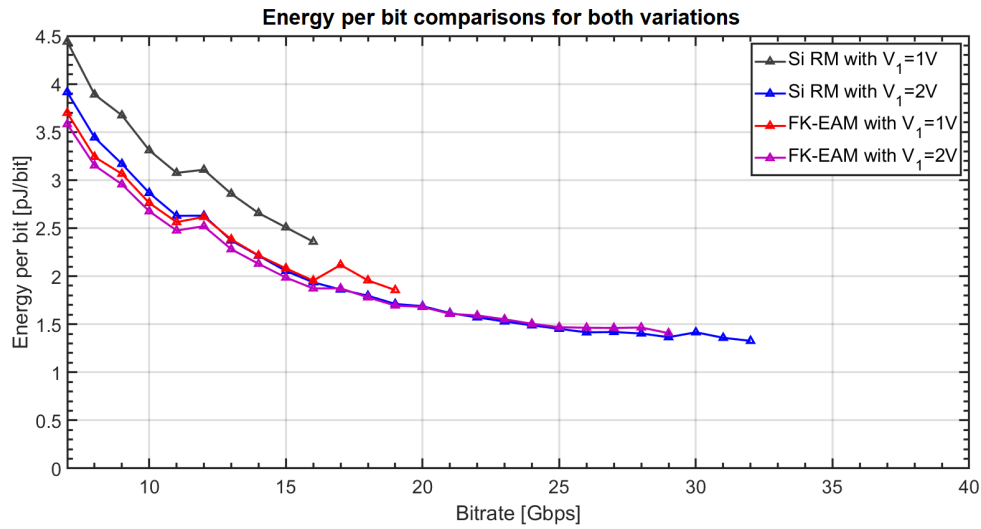
Fig. 6.1 The optical link system energy consumption per bit for the two optical modulators considering both temperature and process variations.

What resulted was that with a driving voltage of 2 V, there is no device that seems to have significantly better performances between the maximum operating bit rates of 15 *Gbps* and 30 *Gbps*.

An important consideration that has to be highlighted again is the fact that the measurements provided came from IMEC demonstrators. However, these measurements do not represent the best performances that these two modulators can achieve, but just some consolidated device performance.

In the end, with the studies presented in sections 4.3 and 4.2, it was possible to obtain the comparisons for the two devices under different conditions. In particular, figure 6.2-a shows only temperature variations, while 6.2-b only process variations. It is evident that in case (a), the Si RM at 2 V slightly performs better, while in case (b) the FK-EAM at 2 V has a lower power consumption. In particular, case (b) has a null heater energy consumption, since there is no need to compensate the 2 *nm* wavelength shift due to its high 1dB optical bandwidth.
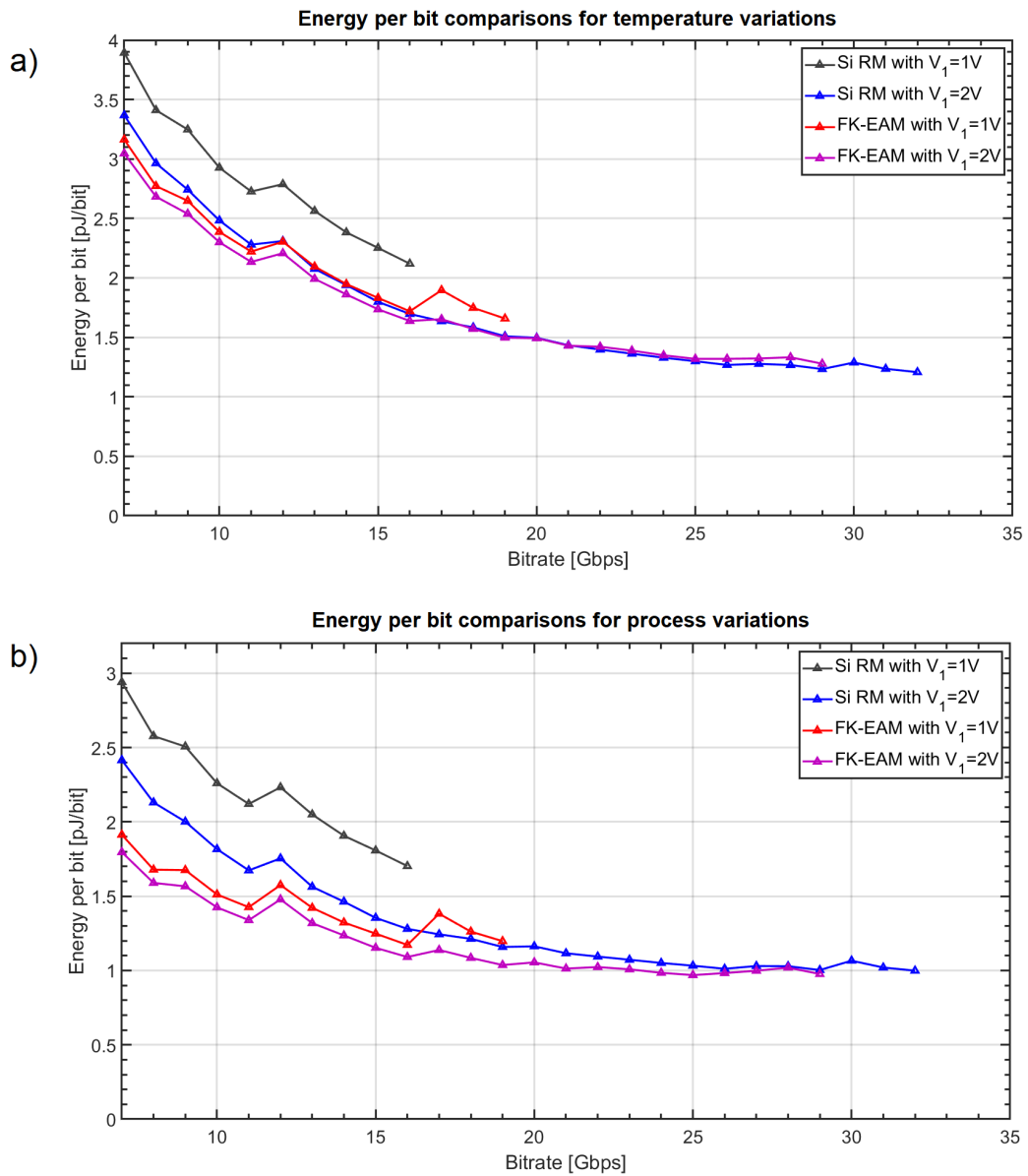
Fig. 6.2 The optical link system energy consumption per bit for the two optical modulators considering the temperature and process variations separately.

6.1 | Future work

The presented work consisted in obtaining models of Si RM and FK-EAM for simulations of optical communications.

For this reason, an interesting study related to this project could be to obtain a model for the QCSE-EAM. In fact, even if this optical modulator was not considered, since it is still an emerging technology, its promising performances make of it an interesting topic to investigate.

Moreover, the communication protocol considered in the optical system was the classic Non-return to zero (NRZ). An alternative for reaching high bandwidth at low energy consumption per bit, could be to implement a Pulse-Amplitude modulation (PAM4) and to compare its performances with the NRZ. In order to perform a PAM4 analysis, different building blocks of the system have to be implemented. For example, for what concerns the optical modulator, a segmented Si RM, or two ring modulators could be used.

In the end, it is important to clarify that the energy consumption per bit study performed, didn't take into account several blocks, that may have an impact in the total consumption. For example, after the TIA, it is present a limiting amplifier that was not considered. Moreover, a block that is necessary for bit rates of 25 *Gbps* and more, is the clock and data recovery (CDR). This block is necessary at these bit rates and it has an high energy consumption per bit of the order of the 2 *pJ/bit* [30], which means almost 50% of the consumption estimated in the link analysis performed in chapter 4.

For accurate estimation of the energy consumption per bit, all those studies have to be done and included in the already-existing framework.

References

[1] F. O'Mahony *et al.*, "The future of electrical I/O for microprocessors". 2009 International Symposium on VLSI Design, Automation and Test, Hsinchu, 2009, pp. 31-34. doi: 10.1109/VDAT.2009.5158087

[2] J. D'Ambrosia *et al.*, "New 2018 Ethernet Roadmap Looks to Future Speeds of 1.6 Terabits/s".April 2013, Ethernet Alliance. (available on Thursday 4th April, 2019: https://insidehpc.com/2018/03/new-2018-ethernet-roadmap-looks-future-speeds-1-6-terabits-s/)

[3] Zip folder with all 2018 Roadmap Graphics, "Ethernet's Terabit Future Seen in New Ethernet Alliance Roadmap". March 13, 2018. Ethernet Alliance. (available on Thursday 4th April, 2019: https://ethernetalliance.org/wp-content/uploads/2016/03/Roadmap-Graphics.zip)

[4] N. Binkert *et al.*, "The role of optics in future high radix switch design". 2011 38th Annual International Symposium on Computer Architecture (ISCA), San Jose, CA, 2011, pp. 437-447.

[5] A. Joshi *et al.*, "Silicon-photonic clos networks for global on-chip communication". 2009 3rd ACM/IEEE International Symposium on Networks-on-Chip, San Diego, CA, 2009, pp. 124-133.doi: 10.1109/NOCS.2009.5071460

[6] M. Rakowski, "CMOS circuitry for low power ring-based silicon photonics optical link," November 2014. Dissertation for the degree of Doctor in Engineering, KU Leuven, Belgium.

[7] D. Guckenberger *et al.* "Advantages of CMOS photonics for future transceiver applications." 36th European Conference and Exhibition on Optical Communication (2010): 1-6.

[8] J.E. Proesel *et al.*, "Ultra-Low-Power 10 to 28.5 Gb/s CMOS-Driven VCSEL-Based Optical Links," OFC/NFOEC, Los Angeles, CA, 2012, pp. 1-3.

[9] S. Gupta *et al.*, "50GHz Ge Waveguide Electro-Absorption Modulator Integrated in a 220 nm SOI Photonics Platform", Imec, Kapeldreef 75, Leuven B-3001, Belgium, 2015.

[10] D.A.B. Miller, *et al.* "Relation between electro absorption in bulk semiconductors and in quantum wells: The quantum-confined Franz Keldysh effect", Phys. Rev. B 33, 6976 (1986)

[11] D. Vermeulen *et al.*, "High-efficiency fiber-to-chip grating couplers realized using an advanced CMOS-compatible Silicon-On-Insulator platform", 2010 OSA 16 August 2010 / Vol. 18, No. 17 / OPTICS EXPRESS 18278

[12] Horizon 2020, Founding programmes. European Commision. (available on Thursday 4th April, 2019: https://ec.europa.eu/programmes/horizon2020/en/h2020-section/photonics)

[13] B. Jalali *et al.*, "Silicon Photonics," in Journal of Lightwave Technology, vol. 24, no. 12, pp. 4600-4615, Dec. 2006. doi: 10.1109/JLT.2006.885782

[14] K. T. Settaluri *et al.*, "First principles optimization of opto-electronic communication links", IEEE Trans. Circuits Syst. I Reg. Papers, vol. 64, no. 5, pp. 1270-1283, May 2017.

[15] W. Bogaerts *et al.*, " Silicon microring resonators". Laser Photonics Rev. 6, No. 1, 4773 (2012) / DOI 10.1002/lpor.201100017

[16] D. A. B. Miller, "Energy consumption in optical modulators for interconnects," Opt. Express 20, A293-A308 (2012)

[17] Sen Lin *et al.*, "Electronic-Photonic Co-Optimization of High-Speed Silicon Photonic Transmitters," J. Lightwave Technol. 35, 4766-4780 (2017)

[18] L. Chrostowski *et al.*, "Modulators" in Silicon Photonics Design: From Devices to Systems, 1st ed. Cambridge, U.K.: Cambridge Univ. Press, 2015.

[19] "Energy Bands and Charge Carriers in Semiconductors - Temperature Dependence of Carrier Concentrations". IIT - Delji. (link available on Thursday 4th April, 2019: https://nptel.ac.in/courses/Webcourse-contents/IIT-Delhi/Semiconductor% 20Devices/LMB2A/2c.htm)

[20] "Principles of Electronic devices - 2.2.5 Temperature dependence of the energy bandgap", Bart J. Van Zeghbroeck, 1996, 1997. (link available Thursday 4th April, 2019on: https://ecee.colorado.edu/~bart/book/eband5.htm)

[21] A. K. Sana *et al.*, "Temperature dependence of resonance characteristics of silicon resonators and thermal stability improvement by differential operation method". Japanese Journal of Applied Physics, vol. 56, N 4S, 2017. (available on Thursday 4th April, 2019: http://stacks.iop.org/1347-4065/56/i=4S/a=04CC06)

[22] J. Liu *et al.*, "Design of monolithically integrated GeSi electro-absorption modulators and photodetectors on an SOI platform," Opt. Express 15, 623-628 (2007)

[23] K. Saraswat *et al.*, "High performance germanium MOSFETs". Materials Science and Engineering: B, 135(3):242 – 249, 2006. E-MRS IUMRS ICEM 2006, Symposium B; From strained silicon to nanotubes - Novel channels for field effect devices.

[24] G. Wang *et al.*, "Selective epitaxial growth of germanium on Si wafers with shallow trench isolation: an approach for Ge virtual substrates." ECS Transactions, 16(10):829–836, 2008.

[25] S.L. Chuang. "Physics of Photonic Devices". Wiley Series in Pure and Applied Optics. John Wiley & Sons, 2009. ISBN:0470293195 9780470293195

[26] Airy function's MATLAB function. Mathworks webpage (link available Thursday 4th April, 2019: https://www.mathworks.com/help/matlab/ref/airy.html)

[27] Physical properties of Germainum. (available on Thursday 4th April, 2019: http://www.ioffe.ru/SVA/NSM/Semicond/Ge/index.html)

[28] S. A. Srinivasan. "Advanced Germanium Devices for Optical Interconnects". Gent University, 2018. ISBN: 978-94-6355-103-8

[29] W. Freude *et al*., "Quality metrics for optical signals: Eye diagram, Q-factor, OSNR, EVM and BER," 2012 14th International Conference on Transparent Optical Networks (ICTON), Coventry, 2012, pp. 1-4. doi: 10.1109/ICTON.2012.6254380

[30] Z. Wang *et al*., "A 25Gbps, 2x-oversampling CDR using a zero-crossing linearizing phase detector," 2014 IEEE Radio Frequency Integrated Circuits Symposium, Tampa, FL, 2014, pp. 271-274. DOI: 10.1109/RFIC.2014.6851717

$\mathcal{A}$ MATLAB code for the Si RM

A.1 | Temperature dependency

In this section is reported the MATLAB function used to evaluate the temperature dependent parameters of the Si-RM, in particular the E_g, the n_i, V_{bi} and $n_{eff,i}$, once having set the RM parameters and the simulation parameters in the relative MATLAB codes.

```matlab
function Temp_param = Temp_dependency_function_RM(sim_param,
    ring_param)

%Constants and coefficients necessary:
q=1.602e-19; % Electron charge [C]
%Eg(T)=Eg0-a*T^2/(T+b), "a,b" fitting parameters for the energy
    gap
Eg_0=1.166*q; % [J], which means 1.166eV
a=4.73e-4*q;   % [J/K], which means 4.73e-4 eV/K
b=636;          % [K]
%Constants needed:
kb=1.38e-23; % Boltzmann constant [J/K]
h=6.6261e-34;% Plank constant [J*s]
coeff=1.308209099875871e-51; % (m_e*m_h)^(3/4)

Temp_param.Eg_T=Eg_0-a*sim_param.T^2/(sim_param.T+b); % Energy gap
    [J]
```

```matlab
15 │ Temp_param.ni_T=2*(2*pi*kb*sim_param.T/h^2)^(3/2)*coeff*exp(-
   │     Temp_param.Eg_T/(2*kb*sim_param.T)); %Intrinsic carrier
   │     concentration [cm^-3]
16 │ Temp_param.V_bi_T=(kb*sim_param.T/q)*log((ring_param.NA*ring_param
   │     .ND)/Temp_param.ni_T^2); %Built-in potential [V]
17 │
18 │ dlam = (sim_param.lambda-ring_param.lambda_0);
19 │ Temp_param.neff_i = ring_param.neff_i0 + dlam*(ring_param.neff_i0-
   │     ring_param.ng)/ring_param.lambda_0-ring_param.delta_neff_vs_T*(
   │     sim_param.T-ring_param.T_0);
20 │ end
```

A.2 | Transfer function

The MATLAB code reported in this section was used to evaluate the transfer function T_n for the Si-RM, once having set the RM parameters and the simulation parameters in the relative MATLAB codes.

```matlab
1 │ function T_n = transfer_function_RM(Temp_param, ring_param,
  │     sim_param);
2 │
3 │     %Sperimental technology_param from: [2] "Electronic - Photonic
4 │     %Co-Optimization of High-Speed Silicon Photonic Transmitters"
  │         - Sen Lin
5 │     %Soref & Bennett, 1987, unit: [cm],
6 │     %fitting technology_param for the n_eff and alpha computation
7 │     A = ring_param.lambda_0^2*3.64e-10;
8 │     B = ring_param.lambda_0^2*3.51e-6;
9 │     C = 1/2*ring_param.lambda_0^2*3.52e-6;
10│     D = 1/2*ring_param.lambda_0^2*2.4e-6;
11│     %Constants:
12│     eps_0=8.854e-14; % Permittivity [F/cm]
13│     eps_r=11.68;
14│     q=1.602e-19; % Electron charge [C]
15│     %Computation of the depletion widths of the n and p doping in
  │         [cm]
```

```matlab
        xn=sqrt((2*eps_0*eps_r*ring_param.NA*(Temp_param.V_bi_T-
            sim_param.V))/(q*ring_param.ND*(ring_param.NA+ring_param.ND
            )));
        xp=sqrt((2*eps_0*eps_r*ring_param.ND*(Temp_param.V_bi_T-
            sim_param.V))/(q*ring_param.NA*(ring_param.NA+ring_param.ND
            )));
        %Compute the eff. refractive index and absorption coeff. vs T,
            lambda
        neff_d=Temp_param.neff_i-(A*ring_param.ND+B*ring_param.NA^0.8)
            /2*ring_param.wf;
        alpha_d=ring_param.alpha_i+100*(C*ring_param.ND+D*ring_param.
            NA)/2*ring_param.wf;
        %Computation of the transfer function T_n=P_tx/P_in
        neff=neff_d+(xp*B*ring_param.NA^0.8 + xn*A*ring_param.ND)/
            ring_param.Lj*ring_param.wf;
        alpha=alpha_d-100*(xp*D*ring_param.NA + xn*C*ring_param.ND)/
            ring_param.Lj*ring_param.wf;
        a=exp(-alpha *ring_param.L); %a is the round trip absorption
        theta=2*pi*ring_param.L*neff /sim_param.lambda ;
        T_n=abs((ring_param.t-a*exp(1i*theta))/(1-ring_param.t*a*exp(1
            i*theta)))^2;

end
```

$\mathcal{B}$ MATLAB code for the FK-EAM

B.1 | Transfer function

The MATLAB code reported in this section was used to evaluate the transfer function T_n for the GeSi FK-EAM, once having set the EAM parameters and the simulation parameters in the relative MATLAB codes.

```matlab
function [Tn] = transfer_function_EAM(EAM_param,sim_param)

        %list of constants
        q = 1.6e-19;
        m_0 = 9.10938356e-31;
        h=6.62607004e-34;
        c=3e8;
        hbar = h/(2*pi);
        EMM = 23*q;
        eps_r = 16.2;

        E_field=(-0.6018*sim_param.V +0.71)./EAM_param.d;
        %The 0.7V of bias was added to fit the model. It makes
        %sense since there is always an absorption, even at 0V
        m_r=EAM_param.mr*m_0;
        E_ph=c*h/sim_param.lambda;
        E_geV =EAM_param.E_g0K -((4.8e-4*sim_param.T^2)/(sim_param.T+235))); % [eV]
        E_g = E_geV*q; % [J]
```

```matlab
            hthf  =  ( hbar ^2*q^2.* E_field .^2/2/m_r) .^(1/3) ;
            A_0  =  2* pi *q^2.*EMM/ sqrt ( eps_r ) / c /8.86 e −12/m_0./E_ph* hbar ;
            eta  =  (E_g−E_ph) ./ hthf ;
            avg  =  3/7;  % averaging , scaling factor
            alpha  =  avg *(A_0/2/ pi ^2) *(2* m_r/hbar ^2) ^(1.5) .* sqrt ( hthf )
                .*(− eta .* airy (0 , eta ) .^2+ airy (1 , eta ) .^2) ;
            Tn=0.5623* exp(− alpha *EAM_param.L) ;

end
```